The Astrophysical Journal, 806:237 (22pp), 2015 June 20 doi:10.1088/0004-637X/806/2/237

PLASMA EMISSION BY NONLINEAR ELECTROMAGNETIC PROCESSES

L. F. Ziebell[1], P. H. Yoon[2,3], L. T. Petruzzellis[1], R. Gaelzer[1], and J. Pavan[4]
[1] Instituto de Física, UFRGS, Porto Alegre, RS, Brazil; luiz.ziebell@ufrgs.br, laripetruzzellis@yahoo.com.br, rudi.gaelzer@ufrgs.br
[2] Institute for Physical Science & Technology, University of Maryland, College Park, USA; yoonp@umd.edu
[3] School of Space Research, Kyung Hee University, Yongin, Korea
[4] Instituto de Física e Matemática, UFPel, Pelotas, RS, Brasil; joel.pavan@ufpel.edu.br
Received 2015 February 13; accepted 2015 March 29; published 2015 June 22

ABSTRACT

The plasma emission, or electromagnetic (EM) radiation at the plasma frequency and/or its harmonic(s), is generally accepted as the radiation mechanism responsible for solar type II and III radio bursts. Identification and characterization of these solar radio burst phenomena were done in the 1950s. Despite many decades of theoretical research since then, a rigorous demonstration of the plasma emission process based upon first principles was not available until recently, when, in a recent Letter, Ziebell et al. reported the first complete numerical solution of EM weak turbulence equations; thus, quantitatively analyzing the plasma emission process starting from the initial electron beam and the associated beam-plasma (or Langmuir wave) instability, as well as the subsequent nonlinear conversion of electrostatic Langmuir turbulence into EM radiation. In the present paper, the same problem is revisited in order to elucidate the detailed physical mechanisms that could not be reported in the brief Letter format. Findings from the present paper may be useful for interpreting observations and full-particle numerical simulations.

Key words: plasmas – radiation mechanisms: non-thermal – solar wind – Sun: radio radiation – turbulence – waves

1. INTRODUCTION

Observations of solar radio emissions in the meter wavelengths and the subsequent classification were done in the 1950s (Wild 1950a, 1950b; Wild & McCready 1950; Wild et al. 1954). Of the various types of solar radio bursts, it was suggested early on that fast electrons escaping from active regions in the Sun may be responsible for the type III radio bursts, and a similar process may also be operative for type II emissions (Roberts 1959; Wild et al. 1959). Both type II and III radio bursts are often associated with the fundamental/harmonic two-band structure, although it is more common for type II bursts than for type III emissions. For the latter, the two-band emissions are actually quite rare. For reviews on the subject of type III radio bursts, see, e.g., Wild et al. (1963), Kundu (1965), Zheleznyakov (1970), Wild & Smerd (1972), Stewart (1974), Fainberg & Stone (1974), Lin (1974), Smerd (1976), Rosenberg (1976), Melrose (1980a, 1980b, 1986), Goldman (1983), Suzuki & Dulk (1985), Dulk (1985), Reiner et al. (1992), Robinson & Cairns (1998a, 1998b, 1998c), Cane et al. (2002), Reiner et al. (2009), and Reid & Ratcliffe (2014).

The first theory of plasma emission and type III radio bursts was proposed in 1958 by Ginzburg & Zheleznyakov (1958), though their original theory has undergone a considerable amount of modifications and improvements over the decades (Tsytovich 1967; Kaplan & Tsytovich 1968; Zheleznyakov & Zaitsev 1970a; Melrose 1982, 1987; Goldman & Dubois 1982; Cairns 1987; Robinson & Cairns 1998a; Li et al. 2005a, 2005b, 2006a, 2006b, 2008a, 2008b, 2009, 2010, 2011a, 2011b, 2011c). Essentially, the standard paradigm of plasma emission first involves energetic electrons produced at the solar active region during the flare. As the energetic electrons stream outward following open magnetic field lines, they interact with the dense background solar wind plasma. The beam-plasma interaction excites Langmuir (L) waves via the well-known bump-on-tail instability, followed by nonlinear processes of wave decay and scattering, eventually leading to the backward-propagating Langmuir waves as well as low-frequency ion-acoustic waves. The generation of electromagnetic (EM) radiation is a byproduct of the nonlinear processes. Partial conversion of electrostatic wave energy, primarily residing in the form of Langmuir turbulence, to transverse EM wave energy is called the plasma emission process, and the resultant radiation emission occurs at the plasma frequency and/or its harmonic(s).

Such an elaborate process can, in principle, be demonstrated on the basis of EM weak turbulence theory,—the fundamental equations thereof and their derivation can be found, e.g., in Yoon (2006), Yoon et al. (2012a), and Ziebell et al. (2014b). Indeed, over the past several decades, the physics of plasma emission was discussed within the framework of reduced or partial EM weak turbulence theory (Li et al. 2005a, 2005b, 2006a, 2006b, 2008a, 2008b, 2009, 2010, 2011a, 2011b, 2011c; Schmidt & Cairns 2012a, 2012b, 2014). However, the complete numerical solution of the entire set of EM weak turbulence equations has not been done until quite recently, when Ziebell et al. (2014a) numerically solved the complete equations of EM weak turbulence theory for the first time. Until then, various approximations and simplifications have been made, which include the assumption of saturated wave amplitudes, the predetermination of certain nonlinear processes as being the most important, the reduction of the equations to one-dimensional models, etc.

We should note, however, that the above comments are not meant to diminish the value and importance of reduced theories. Some of these theories, especially those from the University of Sydney (Li et al. 2005a, 2005b, 2006a, 2006b, 2008a, 2008b, 2009, 2010, 2011a, 2011b, 2011c; Schmidt & Cairns 2012a, 2012b, 2014), have advanced to the point where simple yet reliable plasma emission models are incorporated into macroscopic models so as to yield global-kinetic models for both type II and type III radio bursts with predictive capabilities. Nevertheless, since reduced models are based upon various assumptions, it is difficult to quantitatively assess the importance of various physical processes. It is desirable to formulate fully general numerical solutions so that one may

establish a benchmark full numerical solution against which more approximate methods can be compared. With such a purpose in mind, Ziebell et al. (2014a) first reported their findings in a Letter format. In the present paper, we revisit the same problem, but we now greatly expand on the detailed discussions of various aspects of the findings, which could not be reported in the brief Letter format.

Before we proceed, it should be mentioned that a few authors carried out direct EM particle-in-cell (PIC) simulations in order to characterize the nonlinear behavior of the plasma emission process (Kasaba et al. 2001; Karlicky & Vandas 2007; Rhee et al. 2009a, 2009b; Ganse et al. 2012a, 2012b). In spite of the significance of full-particle simulation, which contains more rigorous physics than any analytical theory, however, it should also be mentioned that simulations of the plasma emission process under realistic conditions is still very challenging due to a number of reasons, including the fact that whereas electrostatic Langmuir waves excited by the beam are characterized by short wavelength, the transverse EM waves have very long wavelengths. Besides, the particle simulation is, strictly speaking, but a computer-simulated experiment that needs to be interpreted. In this regard, the present full numerical solution of the analytical EM weak turbulence equations is complementary to PIC simulation efforts.

2. THEORETICAL FORMALISM

The wave intensities for plasma eigen-modes, Langmuir (L), ion-sound, or equivalently, ion-acoustic (S), and transverse EM (T) modes, are defined by their spectral electric and magnetic field energy intensities. For longitudinal electrostatic modes, i.e., the Langmuir and ion-sound modes, the intensities $I_{\boldsymbol{k}}^{\sigma\alpha}$ for $\alpha = L, S$ are defined by

$$\left\langle \delta E_{\parallel}^{2} \right\rangle_{\boldsymbol{k},\omega} = \sum_{\sigma=\pm 1} \sum_{\alpha=L,S} I_{\boldsymbol{k}}^{\sigma\alpha} \delta\left(\omega - \sigma\omega_{\boldsymbol{k}}^{\alpha}\right). \tag{1}$$

The electric field spectral intensity for the transverse mode T is defined by

$$\left\langle \delta E_{\perp}^{2} \right\rangle_{\boldsymbol{k}\omega} = \sum_{\sigma=\pm 1} I_{\boldsymbol{k}}^{\sigma T} \; \delta\left(\omega - \sigma\omega_{\boldsymbol{k}}^{T}\right), \tag{2}$$

while the magnetic field intensity is given by

$$\left\langle \delta B^{2} \right\rangle_{\boldsymbol{k}\omega} = \left| \frac{ck}{\omega} \right|^{2} \left\langle \delta E_{\perp}^{2} \right\rangle_{\boldsymbol{k}\omega}. \tag{3}$$

The linear dispersion relations in (1) and (2) for electrostatic (Langmuir L and ion-sound S) and transverse EM (T) modes are given by

$$\begin{aligned} \omega_{\boldsymbol{k}}^{L} &= \omega_{\mathrm{pe}}\left(1 + \frac{3}{2}k^{2}\lambda_{D}^{2}\right), \\ \omega_{\boldsymbol{k}}^{S} &= kc_{S}\left(1 + \frac{3T_{e}}{T_{i}}\right)^{1/2} \frac{1}{\left(1 + k^{2}\lambda_{D}^{2}\right)^{1/2}}, \\ \omega_{\boldsymbol{k}}^{T} &= \left(\omega_{\mathrm{pe}}^{2} + c^{2}k^{2}\right)^{1/2}, \end{aligned} \tag{4}$$

where

$$\omega_{\mathrm{pe}} = \left(\frac{4\pi n_{e} e^{2}}{m_{e}}\right)^{1/2} \tag{5}$$

is the plasma frequency, n_e, e, and m_e being the electron number density, unit electric charge, and electron mass, respectively,

$$\lambda_{D} = \left(\frac{T_{e}}{4\pi n_{e} e^{2}}\right)^{1/2} = \frac{v_{\mathrm{th}}}{\sqrt{2}\,\omega_{\mathrm{pe}}}, \tag{6}$$

is the Debye length, T_e and T_i are electron and ion temperatures, respectively, and

$$v_{\mathrm{th}} = \left(\frac{2T_{e}}{m_{e}}\right)^{1/2} \quad \text{and} \quad c_{S} = \left(\frac{T_{e}}{m_{i}}\right)^{1/2} \tag{7}$$

represent the electron thermal speed and ion-sound speed, m_i being the ion (proton) mass.

For basic derivations of the foundational equations to be presented next, see Yoon (2000, 2005, 2006) and Yoon et al. (2012a). Similar equations can also be found in Ziebell et al. (2008a, 2008b, 2011, 2012, 2014a, 2014b, 2014c). The set of dynamical equations that constitute the EM weak turbulence theory are displayed next. First, the L mode wave kinetic equation is given by

$$\begin{aligned} \frac{\partial I_{\boldsymbol{k}}^{\sigma L}}{\partial t} = {} & \frac{4\pi e^{2}}{m_{e}k^{2}} \int d\boldsymbol{v}\delta\left(\sigma\omega_{\boldsymbol{k}}^{L} - \boldsymbol{k}\cdot\boldsymbol{v}\right) \\ & \times \left(n_{e}e^{2}F_{e}(\boldsymbol{v}) + \pi\sigma\omega_{\boldsymbol{k}}^{L}\boldsymbol{k}\cdot\frac{\partial F_{e}(\boldsymbol{v})}{\partial \boldsymbol{v}} I_{\boldsymbol{k}}^{\sigma L}\right) \\ & + \sum_{\sigma',\sigma''=\pm 1} \int d\boldsymbol{k}' V_{\boldsymbol{k},\boldsymbol{k}'}^{L} \left(\frac{\sigma\omega_{\boldsymbol{k}}^{L} I_{\boldsymbol{k}'}^{\sigma' L} I_{\boldsymbol{k}-\boldsymbol{k}'}^{\sigma'' S}}{\mu_{\boldsymbol{k}-\boldsymbol{k}'}} \right. \\ & \left. - \frac{\sigma'\omega_{\boldsymbol{k}'}^{L} I_{\boldsymbol{k}-\boldsymbol{k}'}^{\sigma'' S} I_{\boldsymbol{k}}^{\sigma L}}{\mu_{\boldsymbol{k}-\boldsymbol{k}'}} - \sigma''\omega_{\boldsymbol{k}-\boldsymbol{k}'}^{L} I_{\boldsymbol{k}'}^{\sigma' L} I_{\boldsymbol{k}}^{\sigma L} \right) \\ & \times \delta\left(\sigma\omega_{\boldsymbol{k}}^{L} - \sigma'\omega_{\boldsymbol{k}'}^{L} - \sigma''\omega_{\boldsymbol{k}-\boldsymbol{k}'}^{S}\right) \\ & + \sum_{\sigma'} \int d\boldsymbol{k}' \int d\boldsymbol{v} U_{\boldsymbol{k},\boldsymbol{k}'}^{L} \\ & \times \left[\frac{n_{e}e^{2}}{\omega_{\mathrm{pe}}^{2}} \left(\sigma\omega_{\boldsymbol{k}}^{L} I_{\boldsymbol{k}'}^{\sigma' L} - \sigma'\omega_{\boldsymbol{k}'}^{L} I_{\boldsymbol{k}}^{\sigma L}\right)\left[F_{e}(\boldsymbol{v}) + F_{i}(\boldsymbol{v})\right] \right. \\ & \left. + \frac{\pi m_{e}}{m_{i}} I_{\boldsymbol{k}'}^{\sigma' L} I_{\boldsymbol{k}}^{\sigma L} (\boldsymbol{k} - \boldsymbol{k}') \cdot \frac{\partial F_{i}(\boldsymbol{v})}{\partial \boldsymbol{v}} \right] \\ & \times \delta\left[\sigma\omega_{\boldsymbol{k}}^{L} - \sigma'\omega_{\boldsymbol{k}'}^{L} - (\boldsymbol{k} - \boldsymbol{k}')\cdot\boldsymbol{v}\right], \end{aligned} \tag{8}$$

where

$$\begin{aligned} V_{\boldsymbol{k},\boldsymbol{k}'}^{L} &= \frac{\pi e^{2}\sigma\omega_{\boldsymbol{k}}^{L}}{2T_{e}^{2}} \frac{\mu_{\boldsymbol{k}-\boldsymbol{k}'}(\boldsymbol{k}\cdot\boldsymbol{k}')^{2}}{k^{2}k'^{2}|\boldsymbol{k}-\boldsymbol{k}'|^{2}}, \\ U_{\boldsymbol{k},\boldsymbol{k}'}^{L} &= \frac{\sigma\omega_{\boldsymbol{k}}^{L} e^{2}}{n_{e}m_{e}^{2}\omega_{\mathrm{pe}}^{2}} \frac{(\boldsymbol{k}\cdot\boldsymbol{k}')^{2}}{k^{2}k'^{2}}, \\ \mu_{\boldsymbol{k}} &= |k|^{3}\lambda_{\mathrm{De}}^{3}\left(\frac{m_{e}}{m_{i}}\right)^{1/2}\left(1 + \frac{3T_{i}}{T_{e}}\right)^{1/2}. \end{aligned} \tag{9}$$

The first velocity integral term on the right-hand side (rhs) of Equation (8), which contains the resonance factor

$\delta(\sigma\omega_k^L - \boldsymbol{k}\cdot\boldsymbol{v})$, represents the spontaneous (the first term within the large parenthesis proportional to F_e) and induced (second terms proportional to $\partial F_e/\partial \boldsymbol{v}$) emissions of L waves. These terms dictate the linear wave-particle interaction as the resonance condition indicates, and physical processes described by these terms are quasilinear processes. The second term that is encompassed by the $\boldsymbol{k}'$-integral designates the three-wave resonance interactions, as indicated by the overall wave–wave resonance delta-function, $\delta(\sigma\omega_k^L - \sigma'\omega_{k'}^L - \sigma''\omega_{k-k'}^S)$. These nonlinear three-wave interaction processes represent the decay/coalescence involving an L mode with another L mode and an S mode. The double integral term $\int d\boldsymbol{v}\int d\boldsymbol{k}'\cdots$, which contains the nonlinear wave-particle resonance condition $\delta[\sigma\omega_k^L - \sigma'\omega_{k'}^L - (\boldsymbol{k}-\boldsymbol{k}')\cdot\boldsymbol{v}]$, represents the spontaneous and induced scattering processes involving two Langmuir waves and the particles. The spontaneous scattering term contains the factor $F_e + F_i$, while the induced scattering term is proportional to the derivative, $\partial F_i/\partial \boldsymbol{v}$.

The wave kinetic equation for the ion-sound mode ($\alpha = S$) is given by

$$\begin{aligned}\frac{\partial}{\partial t}\frac{I_k^{\sigma S}}{\mu_k} &= \frac{4\pi\mu_k e^2}{m_e k^2}\int d\boldsymbol{v}\delta\left(\sigma\omega_k^S - \boldsymbol{k}\cdot\boldsymbol{v}\right)\\ &\times\left[n_e e^2\left[f_e(\boldsymbol{v}) + f_i(\boldsymbol{v})\right]\right.\\ &\left.+\ \pi\sigma\omega_k^L\left(\boldsymbol{k}\cdot\frac{\partial f_e(\boldsymbol{v})}{\partial \boldsymbol{v}} + \frac{m_e}{m_i}\boldsymbol{k}\cdot\frac{\partial f_i(\boldsymbol{v})}{\partial \boldsymbol{v}}\right)\frac{I_k^{\sigma S}}{\mu_k}\right]\\ &+\sum_{\sigma',\sigma''}\int d\boldsymbol{k}' V_{k,k'}^S\left(\sigma\omega_k^L I_{k'}^{\sigma' L} I_{k-k'}^{\sigma'' L}\right.\\ &\left.-\ \frac{\sigma'\omega_{k'}^L I_{k-k'}^{\sigma'' L} I_k^{\sigma S}}{\mu_k} - \frac{\sigma''\omega_{k-k'}^L I_{k'}^{\sigma' L} I_k^{\sigma S}}{\mu_k}\right)\\ &\times\delta\left(\sigma\omega_k^S - \sigma'\omega_{k'}^L - \sigma''\omega_{k-k'}^L\right),\end{aligned} \tag{10}$$

where

$$V_{k,k'}^S = \frac{\pi e^2\sigma\omega_k^L}{4T_e^2}\frac{\mu_k\left[\boldsymbol{k}'\cdot\left(\boldsymbol{k}-\boldsymbol{k}'\right)\right]^2}{k^2k'^2|\boldsymbol{k}-\boldsymbol{k}'|^2}. \tag{11}$$

The first term on the rhs dictated by the velocity integral in Equation (10) corresponds to the spontaneous and induced emissions of S waves. The two processes are quasilinear in nature in that they are depicted by the linear wave-particle resonance factor $\delta(\sigma\omega_k^S - \boldsymbol{k}\cdot\boldsymbol{v})$. The nonlinear terms with the associated $\boldsymbol{k}'$-integral are governed by the three-wave resonance condition $\delta(\sigma\omega_k^S - \sigma'\omega_{k'}^L - \sigma''\omega_{k-k'}^S)$. The nonlinear processes of interest, as far as the present S mode is concerned, are the decay/coalescence involving an S mode with two L modes. We do not consider nonlinear wave-particle interactions (that is, spontaneous and induced scattering processes) involving two S mode waves and the particles since such processes are inefficient and slow in time.

The wave kinetic equation for the transverse mode T is given by

$$\begin{aligned}\frac{\partial}{\partial t}\frac{I_k^{\sigma T}}{2} &= \sum_{\sigma',\sigma''}\int d\boldsymbol{k}' V_{k,k'}^{TLL}\left(\sigma\omega_k^T I_{k'}^{\sigma' L} I_{k-k'}^{\sigma'' L}\right.\\ &\left.-\ \frac{\sigma'\omega_{k'}^L I_{k-k'}^{\sigma'' L} I_k^{\sigma T}}{2} - \frac{\sigma''\omega_{k-k'}^L I_{k'}^{\sigma' L} I_k^{\sigma T}}{2}\right)\\ &\times\delta\left(\sigma\omega_k^T - \sigma'\omega_{k'}^L - \sigma''\omega_{k-k'}^L\right)\\ &+\sum_{\sigma',\sigma''}\int d\boldsymbol{k}' V_{k,k'}^{TLS}\left(\frac{\sigma\omega_k^T I_{k'}^{\sigma' L} I_{k-k'}^{\sigma'' S}}{\mu_{k-k'}}\right.\\ &\left.-\ \frac{\sigma'\omega_{k'}^L I_{k-k'}^{\sigma'' S} I_k^{\sigma T}}{2\mu_{k-k'}^S} - \frac{\sigma''\omega_{k-k'}^L I_{k'}^{\sigma' L} I_k^{\sigma T}}{2}\right)\\ &\times\delta\left(\sigma\omega_k^T - \sigma'\omega_{k'}^L - \sigma''\omega_{k-k'}^S\right)\\ &+\sum_{\sigma',\sigma''}\int d\boldsymbol{k}' V_{k,k'}^{TTL}\left(\frac{\sigma\omega_k^T I_{k'}^{\sigma' T} I_{k-k'}^{\sigma'' L}}{2}\right.\\ &\left.-\ \frac{\sigma'\omega_{k'}^T I_{k-k'}^{\sigma'' L} I_k^{\sigma T}}{2} - \frac{\sigma''\omega_{k-k'}^L I_{k'}^{\sigma' T} I_k^{\sigma T}}{4}\right)\\ &\times\delta\left(\sigma\omega_k^T - \sigma'\omega_{k'}^T - \sigma''\omega_{k-k'}^L\right)\\ &+\sum_{\sigma'}\int d\boldsymbol{k}'\int d\boldsymbol{v} U_{k,k'}^T\left[\frac{\hat{n}e^2}{\omega_{\rm pe}^2}\left(\sigma\omega_k^T I_{k'}^{\sigma' L}\right.\right.\\ &\left.\left.-\ \sigma'\omega_{k'}^L\frac{I_k^{\sigma T}}{2}\right)\left[F_e(\boldsymbol{v}) + F_i(\boldsymbol{v})\right]\right.\\ &\left.+\ \pi\frac{m_e}{m_i}I_{k'}^{\sigma' L}\frac{I_k^{\sigma T}}{2}\left(\boldsymbol{k}-\boldsymbol{k}'\right)\cdot\frac{\partial F_i(\boldsymbol{v})}{\partial \boldsymbol{v}}\right]\\ &\times\delta\left[\sigma\omega_k^T - \sigma'\omega_{k'}^L - \left(\boldsymbol{k}-\boldsymbol{k}'\right)\cdot\boldsymbol{v}\right],\end{aligned} \tag{12}$$

where

$$\begin{aligned}V_{k,k'}^{TLL} &= \frac{\pi e^2\sigma\omega_k^T}{32m_e^2\omega_{\rm pe}^2}\frac{\left(\boldsymbol{k}\times\boldsymbol{k}'\right)^2}{k^2k'^2|\boldsymbol{k}-\boldsymbol{k}'|^2}\left(\frac{k'^2}{\sigma'\omega_{k'}^L} - \frac{|\boldsymbol{k}-\boldsymbol{k}'|^2}{\sigma''\omega_{k-k'}^L}\right)^2,\\ V_{k,k'}^{TLS} &= \frac{\pi e^2\sigma\omega_k^T}{4T_e^2}\frac{\mu_{k-k'}\left(\boldsymbol{k}\times\boldsymbol{k}'\right)^2}{k^2k'^2|\boldsymbol{k}-\boldsymbol{k}'|^2},\\ V_{k,k'}^{TTL} &= \frac{\pi e^2\sigma\omega_k^T}{4m_e^2}\frac{|\boldsymbol{k}-\boldsymbol{k}'|^2}{\left(\omega_k^T\right)^2\left(\omega_{k'}^T\right)^2}\left(1 + \frac{\left(\boldsymbol{k}\cdot\boldsymbol{k}'\right)^2}{k^2k'^2}\right),\\ U_{k,k'}^T &= \frac{\sigma\omega_k^T e^2}{2\hat{n}m_e^2\omega_{\rm pe}^2}\frac{\left(\boldsymbol{k}\times\boldsymbol{k}'\right)^2}{k^2k'^2}.\end{aligned} \tag{13}$$

It is seen that there is no contribution from terms related to spontaneous and induced emissions (quasilinear effects). This is because the linear wave-particle resonance between the T mode and the particles is impossible since no particles can have speeds greater than the speed of light in vacuo. From such a physical ground, the linear wave-particle resonance terms are ignored at the outset. The first $\boldsymbol{k}'$-integral terms on the rhs of Equation (12) dictated by the three-wave resonance condition

$\delta(\sigma\omega_{\boldsymbol{k}}^{T} - \sigma'\omega_{\boldsymbol{k}'}^{L} - \sigma''\omega_{\boldsymbol{k}-\boldsymbol{k}'}^{L})$ represent the coalescence of two L modes into a T mode at the second harmonic plasma frequency, which is conveniently symbolized in the literature by $L + L \leftrightarrow T$. This process is responsible for the (second) harmonic emission with the T mode emission near twice the plasma frequency $\omega \sim 2\omega_{\rm pe}$. The next $\boldsymbol{k}'$-integral associated with the wave–wave resonance factor $\delta(\sigma\omega_{\boldsymbol{k}}^{T} - \sigma'\omega_{\boldsymbol{k}'}^{L} - \sigma''\omega_{\boldsymbol{k}-\boldsymbol{k}'}^{S})$ describes the decaying of an L mode into an S mode and a T mode at the fundamental plasma frequency, $\omega \sim \omega_{\rm pe}$. This is one of the processes that is responsible for the fundamental emission, which is conveniently symbolized in the literature by $T \leftrightarrow L + S$. The third $\boldsymbol{k}'$-integral with the resonance delta function $\delta(\sigma\omega_{\boldsymbol{k}}^{T} - \sigma'\omega_{\boldsymbol{k}'}^{T} - \sigma''\omega_{\boldsymbol{k}-\boldsymbol{k}'}^{L})$ describes the merging of a T mode and an L mode into the next higher harmonic T mode $(T \leftrightarrow T + L)$, which is known as the incoherent Raman scattering process. This term is responsible for generating higher-harmonic plasma emission, especially the third harmonic emission, $\omega \sim 3\omega_{\rm pe}$. The double integral term $\int d\boldsymbol{v}\int d\boldsymbol{k}'\cdots$ dictated by the nonlinear wave-particle resonance condition $\delta[\sigma\omega_{\boldsymbol{k}}^{T} - \sigma'\omega_{\boldsymbol{k}'}^{L} - (\boldsymbol{k} - \boldsymbol{k}')\cdot\boldsymbol{v}]$ represents the spontaneous and induced scattering processes involving T and L modes and the charged particles, ions and electrons. This process is dominated by thermal protons $(T \leftrightarrow p + L)$, as the induced scattering contains only the proton contribution. However, the electrons also contribute $(T \leftrightarrow e + L)$ through the spontaneous scattering. The entire process dictated by the nonlinear wave-particle resonance $\sigma\omega_{\boldsymbol{k}}^{T} - \sigma'\omega_{\boldsymbol{k}'}^{L} - (\boldsymbol{k} - \boldsymbol{k}')\cdot\boldsymbol{v} = 0$ represents an alternative mechanism for the fundamental emission. The complete T mode equation given by (12) has not been solved in conjunction with equations for L and S modes and the particles before, until Ziebell et al. (2014a).

The formal particle kinetic equation is given by

$$\frac{\partial F_a(\boldsymbol{v})}{\partial t} = \frac{\pi e_a^2}{m_a^2}\sum_{\sigma=\pm1}\sum_{\alpha=L,S}\int d\boldsymbol{k}\frac{\boldsymbol{k}}{k}\cdot\frac{\partial}{\partial\boldsymbol{v}}\delta\left(\sigma\omega_{\boldsymbol{k}}^{\alpha} - \boldsymbol{k}\cdot\boldsymbol{v}\right) \times\left(\frac{m_a\mu_{\boldsymbol{k}}^{\alpha}\sigma\omega_{\boldsymbol{k}}^{L}}{4\pi^2 k}F_a(\boldsymbol{v}) + I_{\boldsymbol{k}}^{\sigma\alpha}\frac{\boldsymbol{k}}{k}\cdot\frac{\partial F_a(\boldsymbol{v})}{\partial\boldsymbol{v}}\right), \tag{14}$$

where $a = i, e$ stands for ions and electrons, respectively, and $\mu_{\boldsymbol{k}}^{L} = 1$ and $\mu_{\boldsymbol{k}}^{S} = \mu_{\boldsymbol{k}}$, as defined by Equation (9). For details on the derivation of Equations (8)–(14), the reader is referred to Yoon (2006) and Yoon et al. (2012a).

We introduce the following normalized quantities and definitions,

$$z \equiv \frac{\omega}{\omega_{\rm pe}},\quad \tau \equiv \omega_{\rm pe}t,\quad \boldsymbol{q} \equiv \frac{\boldsymbol{k}v_{\rm th}}{\omega_{\rm pe}},\quad \boldsymbol{u} \equiv \frac{\boldsymbol{v}}{v_{\rm th}},$$
$$\mu_{\boldsymbol{q}}^{L} = 1,\quad \mu_{\boldsymbol{q}}^{T} = 1,\quad \mu_{\boldsymbol{q}}^{S} = \frac{q^3}{2^{3/2}}\sqrt{\frac{m_e}{m_i}}\left(1 + \frac{3T_i}{T_e}\right)^{1/2},$$
$$g = \frac{1}{2^{3/2}(4\pi)^2 n_e\lambda_{\rm De}^3}, \tag{15}$$

as well as the normalized particle velocity distribution function (VDF) and normalized wave spectra,

$$\Phi_a(\boldsymbol{u}) = v_{\rm th}^3 F_a(\boldsymbol{v}),\qquad \mathcal{E}_{\boldsymbol{q}}^{\sigma\alpha} = \frac{(2\pi)^2 g}{m_e v_{\rm th}^2}\frac{I_{\boldsymbol{k}}^{\sigma\alpha}}{\mu_{\boldsymbol{k}}^{\alpha}}. \tag{16}$$

For the purpose of numerical analysis, we rewrite the basic set of self-consistent equations of EM weak turbulence theory (8)–(14) in non-dimensional forms. The equation for the L wave is as follows:

$$\frac{\partial\mathcal{E}_{\boldsymbol{q}}^{\sigma L}}{\partial\tau} = \left\{\frac{\pi\mu_{\boldsymbol{q}}^{L}}{q^2}\int d\boldsymbol{u}\delta\left(\sigma z_{\boldsymbol{q}}^{L} - \boldsymbol{q}\cdot\boldsymbol{u}\right) \times\left(g\Phi_e(\boldsymbol{u}) + \left(\sigma z_{\boldsymbol{q}}^{L}\right)\boldsymbol{q}\cdot\frac{\partial\Phi_e(\boldsymbol{u})}{\partial\boldsymbol{u}}\mathcal{E}_{\boldsymbol{q}}^{\sigma L}\right)\right\}_{Lql} \tag{17a}$$

$$+\left\{2\sigma\mu_{\boldsymbol{q}}^{L}z_{\boldsymbol{q}}^{L}\sum_{\sigma',\sigma''=\pm1}\int d\boldsymbol{q}'\frac{\mu_{\boldsymbol{q}'}^{L}\mu_{\boldsymbol{q}-\boldsymbol{q}'}^{S}(\boldsymbol{q}\cdot\boldsymbol{q}')^2}{q^2q'^2|\boldsymbol{q}-\boldsymbol{q}'|^2} \times\left[\sigma z_{\boldsymbol{q}}^{L}\mathcal{E}_{\boldsymbol{q}'}^{\sigma' L}\mathcal{E}_{\boldsymbol{q}-\boldsymbol{q}'}^{\sigma'' S} - \left(\sigma' z_{\boldsymbol{q}'}^{L}\mathcal{E}_{\boldsymbol{q}-\boldsymbol{q}'}^{\sigma'' S} + \sigma'' z_{\boldsymbol{q}-\boldsymbol{q}'}^{L}\mathcal{E}_{\boldsymbol{q}'}^{\sigma' L}\right)\mathcal{E}_{\boldsymbol{q}}^{\sigma L}\right] \times\delta\left(\sigma z_{\boldsymbol{q}}^{L} - \sigma' z_{\boldsymbol{q}'}^{L} - \sigma'' z_{\boldsymbol{q}-\boldsymbol{q}'}^{S}\right)\right\}_{LdLS} \tag{17b}$$

$$+\left\{\sigma z_{\boldsymbol{q}}^{L}\sum_{\sigma'=\pm1}\int d\boldsymbol{q}'\int d\boldsymbol{u}\frac{\mu_{\boldsymbol{q}}^{L}\mu_{\boldsymbol{q}'}^{L}(\boldsymbol{q}\cdot\boldsymbol{q}')^2}{q^2q'^2} \times\left[g\left(\sigma z_{\boldsymbol{q}}^{L}\mathcal{E}_{\boldsymbol{q}'}^{\sigma' L} - \sigma' z_{\boldsymbol{q}'}^{L}\mathcal{E}_{\boldsymbol{q}}^{\sigma L}\right)\left[\Phi_e(\boldsymbol{u}) + \Phi_i(\boldsymbol{u})\right] + \frac{m_e}{m_i}\mathcal{E}_{\boldsymbol{q}'}^{\sigma' L}\mathcal{E}_{\boldsymbol{q}}^{\sigma L}(\boldsymbol{q}-\boldsymbol{q}')\cdot\frac{\partial\Phi_i(\boldsymbol{u})}{\partial\boldsymbol{u}}\right] \times\delta\left[\sigma z_{\boldsymbol{q}}^{L} - \sigma' z_{\boldsymbol{q}'}^{L} - (\boldsymbol{q}-\boldsymbol{q}')\cdot\boldsymbol{u}\right]\right\}_{LsLL}. \tag{17c}$$

For S mode, the dynamical equation is the following:

$$\frac{\partial\mathcal{E}_{\boldsymbol{q}}^{\sigma S}}{\partial\tau} = \left\{\frac{\pi\mu_{\boldsymbol{q}}^{S}}{q^2}\int d\boldsymbol{u}\delta\left(\sigma z_{\boldsymbol{q}}^{S} - \boldsymbol{q}\cdot\boldsymbol{u}\right)\left[g\left[\Phi_e(\boldsymbol{u}) + \Phi_i(\boldsymbol{u})\right] + \sigma z_{\boldsymbol{q}}^{L}\left(\boldsymbol{q}\cdot\frac{\partial\Phi_e(\boldsymbol{u})}{\partial\boldsymbol{u}} + \frac{m_e}{m_i}\boldsymbol{q}\cdot\frac{\partial\Phi_i(\boldsymbol{u})}{\partial\boldsymbol{u}}\right)\mathcal{E}_{\boldsymbol{q}}^{\sigma S}\right]\right\}_{Sql} \tag{18a}$$

$$+\left\{\sigma z_{\boldsymbol{q}}^{L}\sum_{\sigma',\sigma''=\pm1}\int d\boldsymbol{q}'\frac{\mu_{\boldsymbol{q}}^{S}\mu_{\boldsymbol{q}'}^{L}\mu_{\boldsymbol{q}-\boldsymbol{q}'}^{L}\left[\boldsymbol{q}'\cdot(\boldsymbol{q}-\boldsymbol{q}')\right]^2}{q^2q'^2|\boldsymbol{q}-\boldsymbol{q}'|^2} \times\left[\sigma z_{\boldsymbol{q}}^{L}\mathcal{E}_{\boldsymbol{q}'}^{\sigma' L}\mathcal{E}_{\boldsymbol{q}-\boldsymbol{q}'}^{\sigma'' L} - \left(\sigma' z_{\boldsymbol{q}'}^{L}\mathcal{E}_{\boldsymbol{q}-\boldsymbol{q}'}^{\sigma'' L} + \sigma'' z_{\boldsymbol{q}-\boldsymbol{q}'}^{L}\mathcal{E}_{\boldsymbol{q}'}^{\sigma' L}\right)\mathcal{E}_{\boldsymbol{q}}^{\sigma S}\right] \times\delta\left(\sigma z_{\boldsymbol{q}}^{S} - \sigma' z_{\boldsymbol{q}'}^{L} - \sigma'' z_{\boldsymbol{q}-\boldsymbol{q}'}^{L}\right)\right\}_{SdLL}, \tag{18b}$$

and for T mode, the dimensionless equation is as follows:

$$\frac{\partial \mathcal{E}_q^{\sigma T}}{\partial \tau} = \left\{ \frac{\sigma \mu_q^T z_q^T}{32} \sum_{\sigma',\sigma''=\pm 1} \int d\boldsymbol{q}' \frac{\mu_{q'}^L \mu_{q-q'}^L (\boldsymbol{q}\times\boldsymbol{q}')^2}{q^2 q'^2 |\boldsymbol{q}-\boldsymbol{q}'|^2} \times \left(\frac{q'^2}{\sigma' z_{q'}^L} - \frac{|\boldsymbol{q}-\boldsymbol{q}'|^2}{\sigma'' z_{q-q'}^L} \right)^2 \left[\sigma 2 z_q^T \mathcal{E}_{q'}^{\sigma' L} \mathcal{E}_{q-q'}^{\sigma'' L} - \left(\sigma' z_{q'}^L \mathcal{E}_{q-q'}^{\sigma'' L} + \sigma'' z_{q-q'}^L \mathcal{E}_{q'}^{\sigma' L} \right) \mathcal{E}_q^{\sigma T} \right] \times \delta\left(\sigma z_q^T - \sigma' z_{q'}^L - \sigma'' z_{q-q'}^L \right) \right\}_{TdLL} \quad (19a)$$

$$+ \left\{ \sigma \mu_q^T z_q^T \sum_{\sigma',\sigma''=\pm 1} \int d\boldsymbol{q}' \frac{\mu_{q'}^L \mu_{q-q'}^S (\boldsymbol{q}\times\boldsymbol{q}')^2}{q^2 q'^2 |\boldsymbol{q}-\boldsymbol{q}'|^2} \times \left[\sigma 2 z_q^T \mathcal{E}_{q'}^{\sigma' L} \mathcal{E}_{q-q'}^{\sigma'' S} - \left(\sigma' z_{q'}^L \mathcal{E}_{q-q'}^{\sigma'' S} + \sigma'' z_{q-q'}^L \mathcal{E}_{q'}^{\sigma' L} \right) \mathcal{E}_q^{\sigma T} \right] \times \delta\left(\sigma z_q^T - \sigma' z_{q'}^L - \sigma'' z_{q-q'}^S \right) \right\}_{TdLS} \quad (19b)$$

$$+ \left\{ \frac{\sigma z_q^T}{8} \sum_{\sigma',\sigma''=\pm 1} \int d\boldsymbol{q}' \frac{|\boldsymbol{q}-\boldsymbol{q}'|^2}{\left(z_q^T\right)^2 \left(z_{q'}^T\right)^2} \left(1 + \frac{(\boldsymbol{q}\cdot\boldsymbol{q}')^2}{q^2 q'^2} \right) \times \left[\sigma 2 z_q^T \mathcal{E}_{q'}^{\sigma' T} \mathcal{E}_{q-q'}^{\sigma'' L} - \left(\sigma' 2 z_{q'}^T \mathcal{E}_{q-q'}^{\sigma'' L} + \sigma'' z_{q-q'}^L \mathcal{E}_{q'}^{\sigma' T} \right) \mathcal{E}_q^{\sigma T} \right] \times \delta\left(\sigma z_q^T - \sigma' z_{q'}^T - \sigma'' z_{q-q'}^L \right) \right\}_{TdTL} \quad (19c)$$

$$+ \left\{ \sigma z_q^T \sum_{\sigma'=\pm 1} \int d\boldsymbol{q}' \int d\boldsymbol{u} \frac{\mu_q^T \mu_{q'}^L (\boldsymbol{q}\times\boldsymbol{q}')^2}{q^2 q'^2} \times \left[g \left(\sigma z_q^T \mathcal{E}_{q'}^{\sigma' L} - \sigma' z_{q'}^L \frac{\mathcal{E}_q^{\sigma T}}{2} \right) \left[\Phi_e(\boldsymbol{u}) + \Phi_i(\boldsymbol{u}) \right] + \frac{m_e}{m_i} \mathcal{E}_{q'}^{\sigma' L} \frac{\mathcal{E}_q^{\sigma T}}{2} (\boldsymbol{q}-\boldsymbol{q}') \cdot \frac{\partial \Phi_i(\boldsymbol{u})}{\partial \boldsymbol{u}} \right] \times \delta\left[\sigma z_q^T - \sigma' z_{q'}^L - (\boldsymbol{q}-\boldsymbol{q}')\cdot\boldsymbol{u} \right] \right\}_{TsTL}. \quad (19d)$$

The above set of equations for the three basic normal modes of an unmagnetized plasma, namely, L, S, and T modes, are to be solved together with the dynamical Equations (14) for the particle distribution functions, which is shown in normalized form as follows.

$$\frac{\partial \Phi_a(\boldsymbol{u})}{\partial \tau} = \frac{e_a^2}{e^2} \frac{m_e^2}{m_a^2} \sum_{\sigma} \sum_{\alpha=L,S} \int d\boldsymbol{q} \left(\frac{\boldsymbol{q}}{q} \cdot \frac{\partial}{\partial \boldsymbol{u}} \right) \mu_q^\alpha \delta\left(\sigma z_q^\alpha - \boldsymbol{q}\cdot\boldsymbol{u} \right) \times \left(g \frac{m_a}{m_e} \frac{\sigma z_q^L}{q} \Phi_a(\boldsymbol{u}) + \mathcal{E}_q^{\sigma\alpha} \frac{\boldsymbol{q}}{q} \cdot \frac{\partial \Phi_a(\boldsymbol{u})}{\partial \boldsymbol{u}} \right). \quad (20)$$

In the above $a = e$ denotes the electrons, and $a = i$ stands for the ions (protons). The dispersion relations for plasma normal modes, Equation (4), are now given in dimensionless form by

$$z_q^L = \left(1 + \frac{3q^2}{2} \right)^{1/2},$$
$$z_q^S = \frac{qA}{\left(1 + q^2/2\right)^{1/2}},$$
$$z_q^T = \left(1 + \frac{c^2}{v_{te}^2} q^2 \right)^{1/2}, \quad (21)$$

where

$$A = \frac{1}{\sqrt{2}} \left(\frac{m_e}{m_i} \right)^{1/2} \left(1 + \frac{3T_i}{T_e} \right)^{1/2}. \quad (22)$$

In Equation (17), which describes the evolution of L mode, we designated the first term on the rhs by enclosing within the large curly brackets and with subscript *Lql* (17*a*). This is meant to indicate that the spontaneous and induced emission effects are "quasilinear" in nature. The second term, which describes the effects of three-wave "decay" involving L and S mode waves is denoted with subscript *LdLS* (17*b*). The third term on the rhs, which depicts the effects of "scattering" involving two L waves and particles, is denoted as *LsLL* (17*c*).

Equation (18) for the S wave contains, on the rhs, the first term enclosed within the large curly brackets and designated by subscript *Sql* (18*a*), which describes "quasilinear" processes (that is, the spontaneous and induced emissions). The second term describes the three-wave "decay" processes involving an S mode and two L waves, and thus is designated by *SdLL* (18*b*).

Finally, the evolution of the T mode, which is described by Equation (19), is governed by various processes. The first term on the rhs describes the merging of two L waves into a T mode at approximately twice the plasma frequency (the harmonic or H emission). This wave–wave merging term, which is the opposite of the "decay" process, is thus denoted as *TdLL* (19*a*). The second term describes the influence of three-wave "decay" process of an L mode into a T mode at approximately the fundamental plasma frequency and an S wave. This is one of the processes that is responsible for the fundamental (F) emission, and is consequently expressed with subscript *TdLS* (19*b*). The third term is denoted by *TdTL*, and is meant to characterize three-wave merging (opposite of "decay") interaction involving one L mode wave and a T mode into higher-harmonic T mode (19*c*), that is, higher than twice the plasma frequency. This term turns out to be responsible for the third-harmonic emission when the electron beam energy is sufficiently high. The fourth and the last term describes the nonlinear "scattering" process involving an L mode wave and a T mode wave at the fundamental, mediated by the particles. This is another process responsible for the fundamental plasma emission, as well as for the background radiation level even in the absence of the electron beam. This term is labeled as *TsTL* (19*d*).

Note that in the wave kinetic equations, those terms associated with the input parameter g correspond to spontaneous emission and/or spontaneous scattering processes. In the equation for the particle distribution functions, the term with the parameter g describes the drag, which arises owing to the effects of spontaneous fluctuations, and the term with the

velocity derivative describes the wave-induced (quasilinear) velocity-space diffusion process.

3. NUMERICAL ANALYSIS

We developed a numerical routine termed the EM weak turbulence simulation code to solve the complete set of dimensionless Equations (17*a*)–(20) in two-dimensional (2D) wave number space and 2D velocity space, by employing a splitting method with a fixed time step for the evolution of the distribution and a Runge–Kutta method with the same fixed time step for the wave equations. We carried out the numerical analysis in 2D since the plasma emission cannot take place in a one-dimensional system. It should be noted that the present 2D approach captures all of the necessary physics, and may be largely equivalent to a fully three-dimensional situation with a cylindrical symmetry. We solved the complete set of equations for initial configuration in which the ions are considered stationary and distributed according to thermal equilibrium model with temperature T_i. The ion distribution in 2D velocity space is given by

$$F_i(\boldsymbol{v}) = \frac{m_i}{2\pi T_i}\exp\left(-\frac{m_i v^2}{2T_i}\right), \tag{23}$$

or in the dimensionless form

$$\Phi_i(\boldsymbol{u}) = \frac{1}{\pi}\frac{T_e}{T_i}\frac{m_i}{m_e}\exp\left(-\frac{m_i}{m_e}\frac{T_e}{T_i}u^2\right). \tag{24}$$

Over the computational time period, we assume that the ions do not undergo any noticeable change, i.e., they are stationary. For the electrons, we assume the presence of a background distribution and a field-aligned beam, as expected, for instance, from single reconnection events leading to particle outflows. Counter-streaming electron beams or different beam distributions with finite pitch angles relative to the magnetic field direction, which may occur in the case of acceleration by shocks, will not be considered in the present analysis (Karlicky & Vandas 2007; Ganse et al. 2012a, 2012b). The electrons are therefore assumed to be initially composed of an isotropic thermal background plus a Gaussian distribution of streaming components. In 2D, this electron distribution is given as follows.

$$F_e(\boldsymbol{v}, 0) = \frac{1 - n_b/n_0}{\pi v_{\rm th}^2}\exp\left(-\frac{v_\perp^2}{v_{\rm th}^2} - \frac{\left(v_\parallel + V_0\right)^2}{v_{\rm th}^2}\right) + \frac{n_b/n_0}{\pi v_{\rm tb}^2}\exp\left(-\frac{v_\perp^2}{v_{\rm tb}^2} - \frac{\left(v_\parallel - V_b\right)^2}{v_{\rm tb}^2}\right). \tag{25}$$

Here, $v_{\rm th} = (2T_e/m_e)^{1/2}$ and $v_{\rm tb} = (2T_{\rm beam}/m_e)^{1/2}$ are the background and forward-beam thermal speeds, respectively, and V_0 and V_b are the drift velocities of the background and the forward beam, respectively. The background drift velocity V_0 is such that it guarantees zero net drift velocity for the electron distribution, i.e.,

$$V_0 = \frac{n_b V_b}{n_0 - n_b}, \tag{26}$$

which preserves the current-free condition. In a dimensionless form, the initial electron distribution (26) is expressed as

$$\Phi_e(\boldsymbol{u}, 0) = \frac{1 - n_b/n_0}{\pi}\exp\left[-u_\perp^2 - \left(u_\parallel + \frac{V_0}{v_{\rm th}}\right)^2\right] + \frac{n_b/n_0}{\pi}\frac{T_e}{T_{\rm beam}}\exp\left\{-\frac{T_e}{T_{\rm beam}}\left[u_\perp^2 + \left(u_\parallel - \frac{V_b}{v_{\rm th}}\right)^2\right]\right\}. \tag{27}$$

The intensities of L and S waves are initialized by balancing the spontaneous and induced emissions, taking into account the background population. The normalized electric field spectral intensities are therefore given by

$$I_{\boldsymbol{k}}^{\sigma L}(0) = \frac{T_e}{4\pi^2}\frac{1}{1 + 3k^2\lambda_{\rm De}^2},$$
$$I_{\boldsymbol{k}}^{\sigma S}(0) = \frac{T_e}{4\pi^2}k^2\lambda_{\rm De}^2\left(\frac{1 + k^2\lambda_{\rm De}^2}{1 + 3k^2\lambda_{\rm De}^2}\right)^{1/2} \times \frac{\int d\boldsymbol{v}\delta\left(\sigma\omega_{\boldsymbol{k}}^S - \boldsymbol{k}\cdot\boldsymbol{v}\right)\left(F_e + F_i\right)}{\int d\boldsymbol{v}\delta\left(\sigma\omega_{\boldsymbol{k}}^S - \boldsymbol{k}\cdot\boldsymbol{v}\right)\left[F_e + \left(T_e/T_i\right)F_i\right]}, \tag{28}$$

or in dimensionless form,

$$\mathcal{E}_{\boldsymbol{q}}^{\sigma L}(0) = \frac{g}{2\left(z_{\boldsymbol{q}}^L\right)^2},$$
$$\mathcal{E}_{\boldsymbol{q}}^{\sigma S}(0) = \frac{g}{2z_{\boldsymbol{q}}^L z_{\boldsymbol{q}}^S}\frac{\exp\left(-\xi_{\boldsymbol{q}}^2\right) + \eta^{1/2}\exp\left(-\eta\xi_{\boldsymbol{q}}^2\right)}{\exp\left(-\xi_{\boldsymbol{q}}^2\right) + \left(T_e/T_i\right)\eta^{1/2}\exp\left(-\eta\xi_{\boldsymbol{q}}^2\right)},$$
$$\xi_{\boldsymbol{q}}^2 = \frac{\left(z_{\boldsymbol{q}}^S\right)^2}{q^2}, \qquad \eta = \frac{m_i}{m_e}\frac{T_e}{T_i}. \tag{29}$$

Note that the forward ($\sigma = +1$) and backward ($\sigma = -1$) propagating initial spectra are assumed to be the same, that is, they are initially isotropic in k. In the numerical analysis to follow, we consider two cases. The first situation is when the T waves are initially absent. This is the customary situation that would be familiar to most plasma physicists, since according to the standard textbook approach, thermal plasma is not supposed to emit superluminal transverse EM radiation in unmagnetized plasmas via the spontaneous emission process. This is because the transverse wave in unmagnetized plasmas has phase speed that exceeds the speed of light *in vacuo*. In fact, this is the reason terms representing quasilinear processes are absent in the wave kinetic equation for T mode wave, as shown in Equation (12) or (19). However, as recently discussed by Ziebell et al. (2014b, 2014c), when nonlinear effects are taken into account, thermal plasmas not only spontaneously emit longitudinal L and S modes, but T mode waves are also spontaneously emitted via the nonlinear spontaneous scattering process. As a matter of fact, among the various terms on the rhs of Equation (12) or (19), the nonlinear scattering term (19*d*) is singularly responsible for the

emission of T mode waves even in quiescent plasmas. Consequently, we will consider a second possible initial configuration in which the T mode intensity is given according to the dictates of the nonlinear spontaneous scattering theory *a la* Ziebell et al. (2014b, 2014c),

$$I_k^{\sigma T}(0) = \frac{T_e}{2\pi^2}\frac{1}{1 + c^2k^2/\omega_{pe}^2}, \tag{30}$$

or in dimensionless form,

$$\mathcal{E}_q^{\sigma T}(0) = \frac{g}{1 + 3q_*^2}, \qquad q_* = \left(\frac{2}{3}\frac{c^2}{v_{th}^2}\right)^2 q. \tag{31}$$

The input parameter g is related to the customary plasma parameter, which is a measure of importance for particle discreteness. Of course, the plasma parameter, which is defined by the inverse of the number of particles in a sphere with a radius equal to the Debye length, must be sufficiently small in order for the system to qualify as a plasma. Nevertheless, the plasma parameter is not exactly zero but finite. We take it to be $1/(n_e\lambda_D^3) = 5 \times 10^{-3}$. In the actual heliospheric environment this number should be much smaller, on the order of 10^{-8} to 10^{-6} or so, but we adopted an unrealistically high value of the plasma parameter in order to facilitate the numerical procedure, since a realistically small number would bring the initial wave level to a very small value, which results in delaying the onset of the linear growth, and therefore the overall evolution.

The ratio of the beam electron density n_b and the background electron density n_0 is assumed to be $n_b/n_0 = 10^{-3}$, throughout the present discussion. Admittedly, such a ratio is higher than what is detected in the typical type III radio burst events, where it can be as low as 10^{-6}, especially near 1 AU. However, we choose to work with the unrealistically robust beam so that numerical computation can be facilitated. We take the beam propagation direction to be along the z axis.

For the numerical analysis to follow, the Gaussian thermal spread associated with the beam is taken to be the same as that of the background electron thermal speed, $T_e = T_{beam}$. The ion-to-electron temperature ratio is taken to be $T_i/T_e = 1/7$. In the solar wind, the ratio T_i/T_e varies. It is generally less than unity, but this ratio can be of an order of unity or even higher (Gurnett et al. 1979; Newbury et al. 1998). In general, it is expected that unless T_i/T_e is small, ion-sound waves may heavily damp, thus prohibiting the three-wave resonant interaction. However, numerical solutions of the equations of the electrostatic weak turbulence theory as well as the electrostatic PIC simulation of the electron beam-plasma instability show that the three-wave interaction involving the S mode waves may still be operative even when T_i/T_e is as high as an order of unity (Yoon et al. 2012b; Rha et al. 2013). We choose the value specified here only because we had adopted such a ratio in our previous studies such that we may directly compare the findings from the present investigation against the previous results (Ziebell et al. 2001, 2008a, 2008b, 2011, 2012).

For all of the numerical examples to be discussed subsequently, we use the normalized time interval $\Delta\tau = 0.1$. We use 2D velocity and wave number space. For the equations for L and S waves, we employ 51×51 grids for $q_\perp$ and $q_\parallel$, with $0 < q_\perp = k_\perp v_{te}/\omega_p < 0.6$, and $0 < q_\parallel = k_\parallel v_{te}/\omega_p < 0.6$. For the equation for the T waves, we employ a 71×71 grid for $q_\perp$ and $q_\parallel$, with the same boundaries, aiming for better resolution. Whenever necessary, we have used interpolation between the two grids. For the velocities, we use a 62×125 grid for the $(u_\perp, u_\parallel) = (v_\perp/v_{th}, v_\parallel/v_{th})$ space, covering the velocity range $0 < u_\perp = v_\perp/v_{th} < 15$ and $-15 < u_\parallel = v_\parallel/v_{th} < 15$. It is assumed that $v_{te}^2/c^2 = 4.0 \times 10^{-3}$. In the low corona of the Sun, the typical electron thermal energy is $\sim 10^2$ eV, so the present choice is approximately equal to the coronal value. For situations near 1 AU, the ratio v_{te}^2/c^2 should be much lower than the value we chose. However, for the sake of convenience, we shall only consider the value of $v_{te}^2/c^2 = 4.0 \times 10^{-3}$. Having laid out the details of the numerical setup, we now begin the analysis by considering three sample cases.

3.1. Case Study 1: $V_b/v_{th} = 6$

In Figures 1–4, we show the numerical solution for the case in which the normalized initial beam speed is $V_b/v_{th} = 6$ (case 1). We have numerically integrated the complete equations up to a normalized time step of $\omega_{pe}t = 2000$. Figure 1 shows the snapshots of the electron VDF at four different time intervals corresponding to $\omega_{pe}t = 100$, 500, 1000, and 2000. The four snapshots are displayed in Figures 1(a)–(d), in the form of filled contour plots, using a logarithmic scale. For the relatively early time $\omega_{pe}t = 100$, one can still see the drifting electron beam distribution, as indicated in Figure 1(a). As time progresses, however, the positive slope in the parallel velocity is reduced as a result of the well-known quasilinear velocity diffusion process (see Equation (20)), and the beam evolves into a broad range of velocity-space plateau.

The quasilinear relaxation of the electron beam associated with the type III radio source has been the focus of intense research in the literature. Observations of energetic electrons associated with type III events have been available (Lin 1970; Frank & Gurnett 1972; Kane 1972; Lin et al. 1972, 1981, 1986, 1996; Ergun et al. 1998; Gosling et al. 2003; Krucker et al. 2007; Wang et al. 2012). The challenge was how to explain the persistence of the beam feature in spite of the rapid relaxation by quasilinear plateau formation. This was known in the early literature as the *Sturrock dilemma* (Sturrock 1964). Later, however, the issue was resolved in the context of the finite physical dimension of the source size, which leads to the beam-reformation via the time-of-flight effects. Thus, the propagation and relaxation of type III electrons either in homogeneous and inhomogeneous media, with or without the effects of finite source size, i.e., the time-of-flight effects, together with the excitation and saturation of Langmuir turbulence, have received extensive discussions in the literature (Sturrock 1964; Zheleznyakov & Zaitsev 1970b; Zaitsev et al. 1972; Papadopoulos et al. 1974, 1975; Takakura & Shibahashi 1976; Magelssen & Smith 1977; Goldstein et al. 1979; Smith et al. 1979; Grognard 1980, 1982, 1985; Muschietti 1990; Mel'nik et al. 1999; Kontar 2001a, 2001b, 2001c; Kontar & Pécsely 2002; Ziebell et al. 2001, 2008a, 2008b, 2012, 2014a, 2014b, 2014c; Li et al. 2003, 2005a, 2005b, 2006a, 2006b, 2006c, 2008a, 2008b, 2009, 2010, 2011a, 2011b, 2011c; Foroutan et al. 2007; Ratcliffe et al. 2012). The present discussion pertains to a uniform plasma such that we only deal with local physics. Nevertheless, the general numerical demonstration of the beam relaxation as shown in Figure 1 is consistent with all previously known physics in that, in the absence of inhomogeneity or time-of-flight effects, the

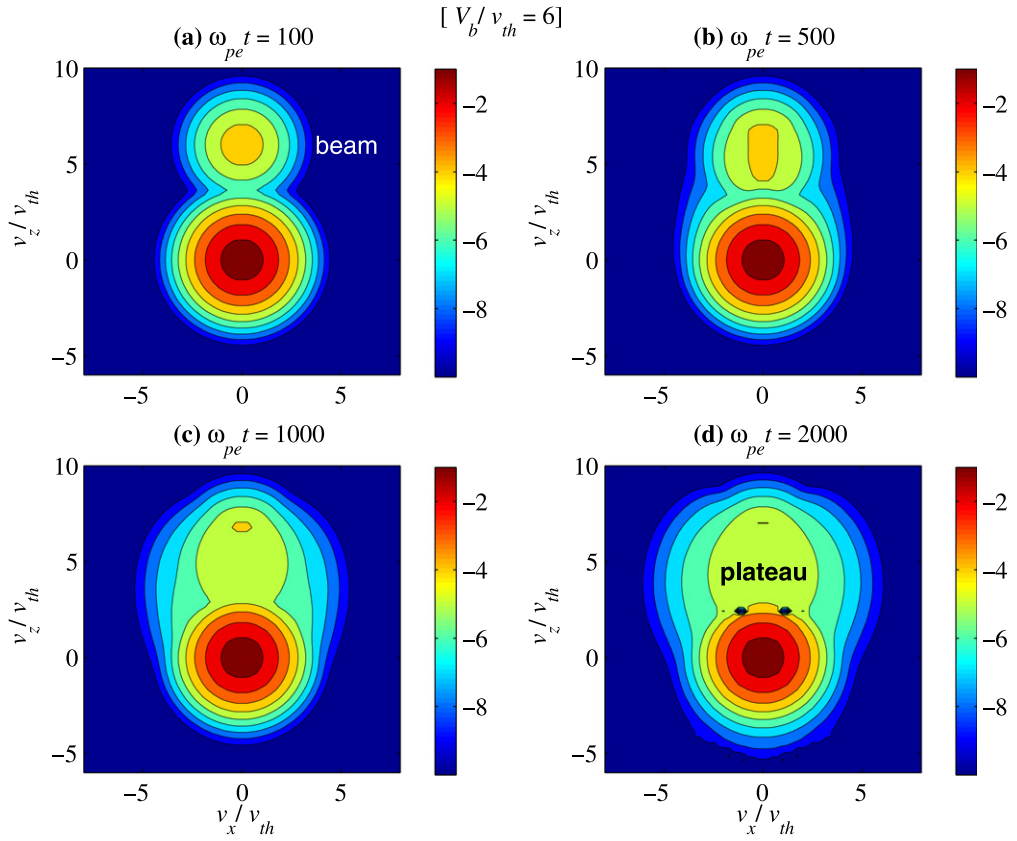

Figure 1. Case 1 ($V_b/v_{\rm th} = 6$): time evolution of the electron velocity distribution function (VDF) F_e (or equivalently Φ_e) vs. $u_\perp = v_x/v_{\rm th}$ and $u_\parallel = v_z/v_{\rm th}$ in filled contour plot format, using a logarithmic scale. Panel (a) shows F_e at a relatively early normalized time $\omega_{\rm pe}t = 100$; panel (b) is for $\omega_{\rm pe}t = 500$; panel (c) shows the snapshot at $\omega_{\rm pe}t = 1000$; and the final panel (d) shows the evolved F_e at $\omega_{\rm pe}t = 2000$.

quasilinear relaxation leads to the formation of the well-known velocity-space plateau.

The Langmuir turbulence spectrum is shown in Figure 2, where it features the spectral intensity $I_L(\boldsymbol{k})$ in normalized form ($\mathcal{E}_{\boldsymbol{q}}^{\sigma L}$) versus $q_\perp$ and $q_\parallel$. The portion of the 2D $\boldsymbol{q}$ space corresponding to $q_\parallel > 0$ is for forward-propagating L mode, $\mathcal{E}_{\boldsymbol{q}}^{+L}$, while the other half space with $q_\parallel < 0$ belongs to the backward L mode, $\mathcal{E}_{\boldsymbol{q}}^{-L}$. We plotted both signs of $\sigma = \pm 1$ in one panel by showing $\mathcal{E}_{\boldsymbol{q}}^{-L}$ in the negative $q_\parallel$ space. Recall that our computational wave number space is for positive $q_\perp$ and positive $q_\parallel$ space. We plotted the negative $q_\perp$ space by simply invoking the symmetry.

For a relatively early time, $\omega_{\rm pe}t = 100$, the enhanced forward-propagating component (the primary L) can be seen to be excited, which is the result of initial bump-on-tail instability (panel a). The physics of early-time evolution for the L mode is governed by Equation (17*a*). For $\omega_{\rm pe}t = 500$, the backscattering of the primary L mode into the oppositely traveling L mode, via a combined three-wave decay process (Equation (17*b*)) and the nonlinear scattering off ions (Equation (17*c*)), becomes visible. For $\omega_{\rm pe}t = 1000$, the primary L mode begins to evolve into a semi-arc shape spectrum. The backscattered L mode was already generated in the form of a ring spectrum even at $\omega_{\rm pe}t = 500$. For the final time step $\omega_{\rm pe}t = 2000$, the total 2D L mode spectrum attains more and more ring-like feature, which was first noticed in our earlier electrostatic weak turbulence calculation (Ziebell et al. 2008a, 2008b, 2012). Note that the present numerical solution of the theoretical equations compares favorably with the simulated spectrum based upon the 2D EM PIC methodology—see, e.g., Figure 2 of (Rhee et al. 2009b).

Nonlinear decay processes that generate the backscattered L mode is accompanied by the production of the ion-sound mode by the same decay instability—see Equation (18*b*), as indicated in Figure 3, which shows the time evolution of the S mode spectral intensity in the same format as Figure 2. Note that the S mode spectral intensity was determined simply by balancing the spontaneous and induced emissions, i.e., by setting Equation (18*a*) to zero. The resulting initial spectrum, given by Equation (28), is rather low in intensity (proportional to g), and is symmetric in k. Figure 3(a) shows the normalized $I_S(\boldsymbol{k})$, or equivalently $\mathcal{E}_{\boldsymbol{q}}^{\sigma S}$, at $\omega_{\rm pe}t = 100$. Because of the fact that the initial beam-plasma system is stable with respect to any instability involving the low-frequency ion-sound mode, the S mode spectrum has not evolved much from its initial configuration. Only at $\omega_{\rm pe}t = 500$ (panel b), the S mode intensity begins to show some evolution. This is the time frame around which the decay instability begins to yield an appreciable level of S mode. The snapshot at $\omega_{\rm pe}t = 1000$ (panel c) shows a slightly more evolved S mode, but even at the end of the computation, namely $\omega_{\rm pe}t = 2000$, the level of S mode remains rather modest. The forward S mode and the moderately enhanced backward S mode are indicated in Figure 3(d).

bFigure 4 corresponds to the transverse EM radiation (T mode) spectrum. We plot the electric field intensity associated with the radiation, $I_T(\boldsymbol{k})$, or in normalized form $\mathcal{E}_{\boldsymbol{q}}^{\sigma T}$, with $\sigma = +1$

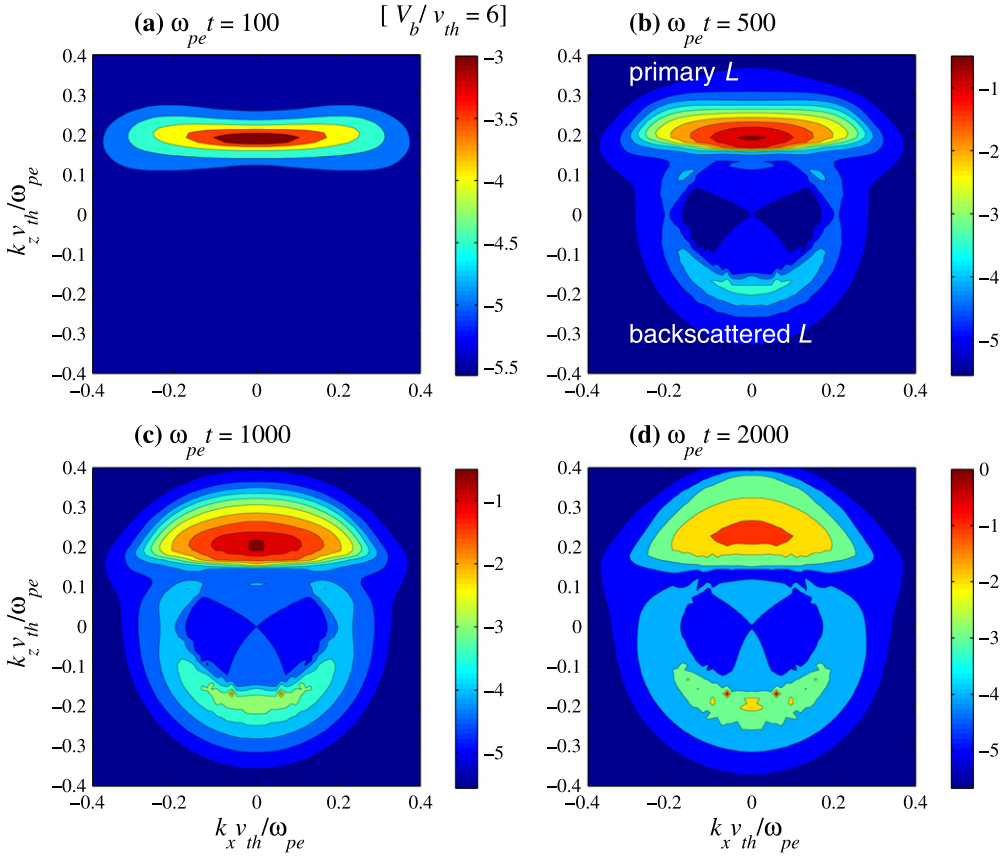

Figure 2. Case 1 ($V_b/v_{\rm th} = 6$): time evolution of the Langmuir wave spectral intensity $I_L(\boldsymbol{k})$ vs. $q_\perp = k_x v_{\rm th}/\omega_{\rm pe}$ and $q_\parallel = k_z v_{\rm th}/\omega_{\rm pe}$. Panel (a) shows $I_L(\boldsymbol{k})$ at $\omega_{\rm pe}t = 100$; panel (b) is for $\omega_{\rm pe}t = 500$; panel (c) is $I_L(\boldsymbol{k})$ at $\omega_{\rm pe}t = 1000$; and the final panel (d) shows $I_L(\boldsymbol{k})$ at $\omega_{\rm pe}t = 2000$.

occupying the positive $k_\parallel$ (or $q_\parallel$) portion of the 2D $\boldsymbol{k}$ space, while in the negative $k_\parallel$, the backward T mode with $\sigma = -1$ is plotted.

In the present case study, we do not impose the finite level of the initial T mode, that is the initial level of T mode as specified by Equation (30) or (31) is not imposed, but rather it is set equal to zero. Since at the initial time there is no spectrum of T waves, the level of the T mode should be zero. However, as soon as the code starts running, the nonlinear scattering process represented by the term in Equation (19*d*) creates the T mode spectrum immediately, so that even at the early stages of time evolution there is a full background of T waves, covering the whole range of wave numbers, as noticed even in the absence of a particle beam (Ziebell et al. 2014c). In fact, the numerical solution shown at $\omega_{\rm pe}t = 100$ already resembles the prediction of Equation (30) or (31) in the region of wavenumber relatively far from $k = 0$, representing the background radiation spectrum that would be present even in the absence of a beam. However, the small enhancement appearing around $k = 0$ is the result of the beam. This peak radiation spectrum at the small k (or long wavelength) region in 2D $\boldsymbol{k}$ space actually corresponds to the fundamental (F) emission with radiation frequency near $\omega_{\rm pe}$. A close visual examination shows that the radiation pattern is that of a dipole. We will examine the detailed radiation emission angle and the underlying mechanism in more detail later, but loosely, the F emission is the result of combined (19*b*) and (19*d*).

Figure 4(b) shows that the T mode spectrum at the small k regime is further enhanced by the time the system evolved to $\omega_{\rm pe}t = 500$, but one may also discern a slight enhancement of harmonic radiation. The outer ring shown in Figures 4(b)–(d) corresponds to the second harmonic (H) emission with frequency in the vicinity of $2\omega_{\rm pe}$. For later time steps, $\omega_{\rm pe}t = 1000$ and 2000, the H component becomes more visible, and it is interesting to note that the emission pattern corresponds to an asymmetric ring in 2D $\boldsymbol{k}$ space. The radiation emission angle will be examined in more detail later, but according to the fundamental theory as described by (19*a*), the H mode emission pattern should be that of a quadrupole in its spectral structure.

3.2. Case Study 2: $V_b/v_{\rm th} = 8$

We next consider a somewhat higher beam speed, namely $V_b/v_{\rm th} = 8$ (case 2). Solutions corresponding to this case are displayed in Figures 5–8, in the form of filled contour plots, using a logarithmic scale. Figure 5 shows the electron VDF, F_e (or Φ_e) at $\omega_{\rm pe}t = 100$, 500, 1000, and 2000, as before. The time evolution is qualitatively similar to case 1 in that for a relatively early time, $\omega_{\rm pe}t = 100$, the electron beam feature is still distinguishable, but for later times, $\omega_{\rm pe}t = 500$ and 1000, the positive slope in $u_\parallel$ gradually disappears, until, for $\omega_{\rm pe}t = 2000$, it is completely gone such that a broad velocity-space plateau is formed in the velocity space formerly occupied by the beam. One can also see that as the beam turns into a plateau, there is an overall heating of the electrons, resulting in a broadening of F_e in the $u_\perp$ direction.

The Langmuir turbulence spectrum for case 2 is shown in Figure 6. For $\omega_{\rm pe}t = 100$, the generation of primary L mode via bump-on-tail instability can be seen in panel (a). As the system

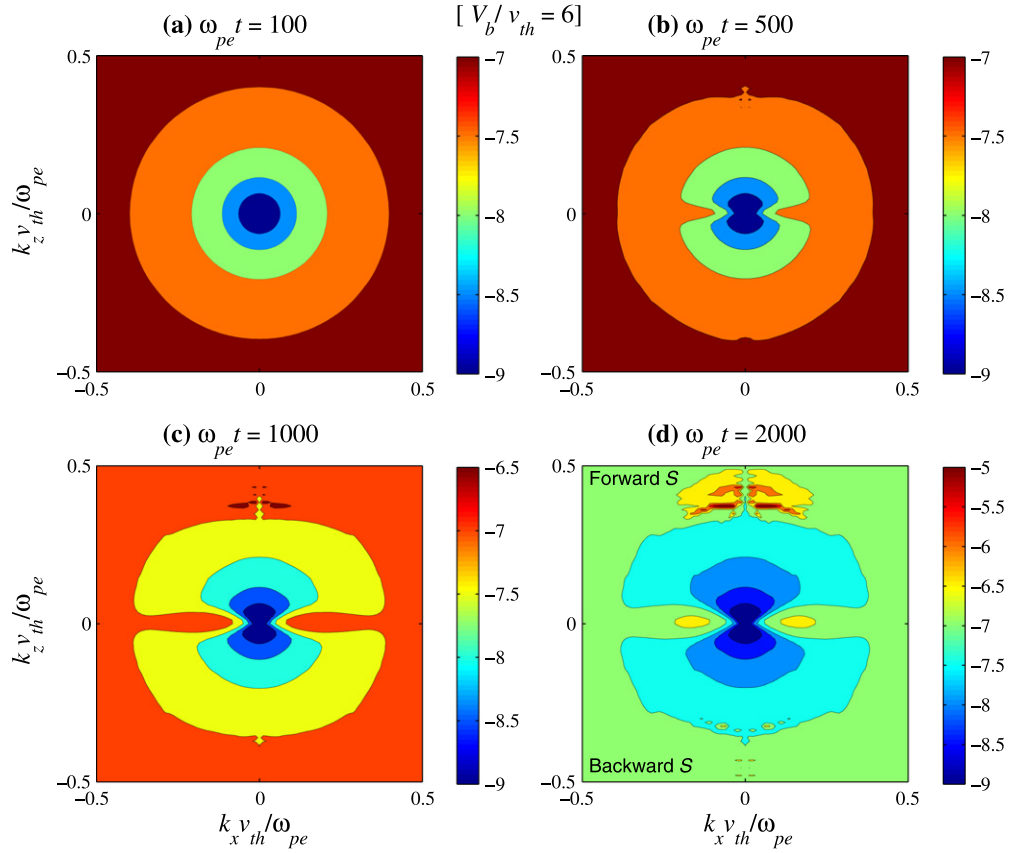

Figure 3. Case 1 ($V_b/v_{\rm th} = 6$): time evolution of the ion-sound wave spectral intensity $I_S(\boldsymbol{k})$ vs. $q_\perp = k_x v_{\rm th}/\omega_{\rm pe}$ and $q_\parallel = k_z v_{\rm th}/\omega_{\rm pe}$. Panel (a) shows $I_S(\boldsymbol{k})$ at $\omega_{\rm pe}t = 100$; panel (b) is for $\omega_{\rm pe}t = 500$; panel (c) is for $\omega_{\rm pe}t = 1000$; and the final panel (d) shows $I_S(\boldsymbol{k})$ at $\omega_{\rm pe}t = 2000$.

evolves to $\omega_{\rm pe}t = 500$, the primary L mode begins to take on a more ring-like morphology in 2D $\boldsymbol{k}$ space, while the backscattered L mode, which takes on the shape of a more symmetric ring spectrum (as compared to the primary L mode) becomes apparent. For $\omega_{\rm pe}t = 1000$, the primary L mode breaks up into a multi-peaked spectrum, along the $k_\parallel$ direction, while also evolving into a more clearly identifiable semi-ring (or semi-arc) spectrum. The backscattered L mode at $\omega_{\rm pe}t = 1000$ evolves into an even more prominent arc-shaped spectrum when compare with the time step at $\omega_{\rm pe}t = 500$. For $\omega_{\rm pe}t = 2000$, the total (primary plus backscattered) 2D L mode spectrum evolved further into a ring-like feature. The reason why the L mode spectrum exhibits a more structured spectrum (along parallel wave number) when compared with case 1 is because of the fact that there is a higher level of free energy associated with the beam in the first place. As a result, nonlinear coupling proceeds faster. The back-and-forth wave–wave and nonlinear wave-particle interactions take place multiple times over the same computational time period in comparison with case 1. Each time L and S modes undergo wave–wave decay and scattering off thermal ions, their wave momenta and energies will become slightly mismatched so as to produce the multiple structured 2D spectra along $k_\parallel$.

The time evolution of the S mode spectral intensity for case 2 is displayed in Figure 7. The S mode spectrum in this case is qualitatively similar to case 1, except that the overall level is enhanced comparatively, and there is more structure associated with the S mode intensity. The physical reason for the multiple structure is the same as already explained above.

Finally, Figure 8 plots the transverse EM radiation (T mode) spectrum for case 2. The present case 2 study also corresponds to the scheme in which we do not impose the finite level of the initial T mode at the outset. Nevertheless, by the time the system evolved to $\omega_{\rm pe}t = 100$, a background level of radiation is already established, similar to that seen in case 1. The overall evolution is similar to case 1 in a loose sense in that the F emission first appears near the origin, followed by the excitation of H emission. The difference in this case is that, as Figure 8(d) shows, the third-harmonic T mode ($3H$) is also visible at $\omega_{\rm pe}t = 2000$. The reason for the excitation of the $3H$ mode is because of the fact that the available particle free energy for case 2 is higher than in the previous case.

3.3. Case Study 3: $V_b/v_{\rm th} = 10$

The third case study is for $V_b/v_{\rm th} = 10$ (case 3). In this high-beam situation, the applicability of weak-growth formula, namely the quasilinear terms in (17*a*), may only be marginally applicable, at least initially. Nevertheless, as the system evolves in time and the free energy, i.e., the beam speed, is reduced, this approach may become more and more appropriate. Numerical solutions corresponding for case 3 are displayed in Figures 9–12 in the form of filled contour plots, using a logarithmic scale. The electron VDF is shown in Figure 9 in the same format as before. In the present case of high initial beam speed, the dynamic evolution is much more rapid when compared with cases 1 and 2. Even for early time $\omega_{\rm pe}t = 100$, the electron beam can be perceived to have already undergone a partial plateau formation. For $\omega_{\rm pe}t = 500$ and 1000, the positive slope in $u_\parallel$ has almost

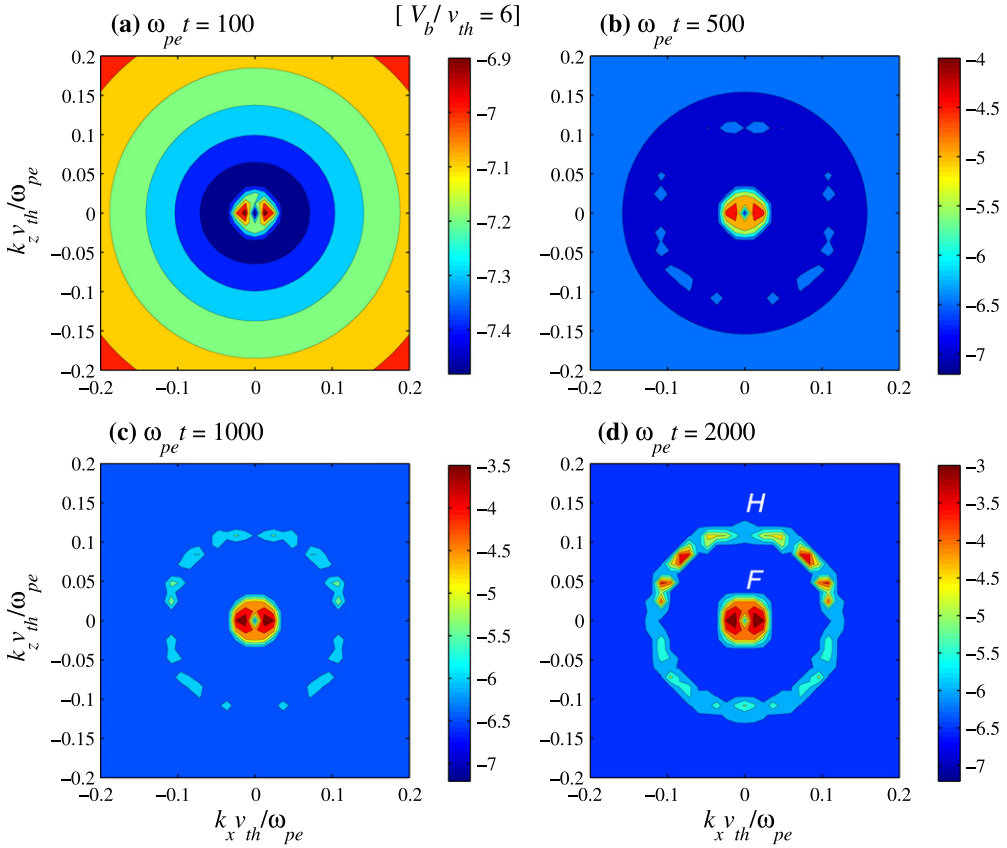

Figure 4. Case 1 ($V_b/v_{\rm th} = 6$): time evolution of the radiation spectral intensity $I_T(\boldsymbol{k})$ vs. $q_\perp = k_x v_{\rm th}/\omega_{\rm pe}$ and $q_\parallel = k_z v_{\rm th}/\omega_{\rm pe}$. Panels (a)–(d) show snapshots of $I_T(\boldsymbol{k})$ at $\omega_{\rm pe} t$ = 100, 500, 1000, and $\omega_{\rm pe} t$ = 2000.

disappeared, except at the boundary that delineates the beam and the background populations. For $\omega_{\rm pe} t = 2000$, the plateau formation has fully progressed, and, in fact, the VDF has spread out (i.e., electrons heated) in all directions, but particularly along $u_\parallel$, such that it reached the velocity-space boundary imposed in the numerical computation.

Figure 10 displays the Langmuir turbulence spectrum for case 3. As with the electron VDF, the time evolution proceeds more rapidly, as expected. The primary L for time step $\omega_{\rm pe} t = 100$ is already seen to have generated weak backscattered L mode (panel a). For later time, $\omega_{\rm pe} t = 500$ (panel b) and 1000 (panel c), it can be seen that the L mode intensity evolves more and more into a symmetric ring spectra in 2D $\boldsymbol{k}$ space, until for $\omega_{\rm pe} t = 2000$, the overall L mode spectrum has become quasi-circular (i.e., quasi-isotropic in k).

The dynamic evolution of the S mode for case 3 is plotted in Figure 11, the S mode spectrum is seen to be appreciably enhanced when compared with the previous two cases, and there is also more structure, indicating repeated back-and-forth wave–wave and nonlinear wave-particle coupling.

Figure 12 displays the radiation (T mode) spectrum for case 3. The dynamic evolution is rapid when compared with other cases, but the most noticeable feature is the fact that the third-harmonic ($3H$) emission level is significant in this case.

Now that we have examined the three sample cases, we next investigate the details of the various physical processes in each case in further detail. The physics of electron-beam, Langmuir, and ion-sound turbulence processes, and in some cases, also the radiation generation processes based upon reduced methods, have been investigated in detail by the present authors in our previous publications as well as by others (Ziebell et al. 2001, 2008a, 2008b, 2011a, 2011b, 2012, 2014a, 2014b, 2014c, Kontar & Pécseli 2002; Li et al. 2003, 2005a, 2005b, 2006a, 2006b, 2006c, 2008a, 2008b, 2009, 2010, 2011a, 2011b, 2011c; Foroutan et al. 2007; Ratcliffe et al. 2012; Schmidt & Cairns 2012a, 2012b, 2014). The novel aspect of the present investigation is the addition of EM effects without recourse to any preliminary assumptions such as one radiation emission mechanism being dominant over others, etc. Although similar previous works on the plasma emission can be found in the literature, mostly by the University of Sydney group (Li et al. 2005a, 2005b, 2006a, 2006b, 2008a, 2008b, 2009, 2010, 2011a, 2011b, 2011c; Schmidt & Cairns 2012a, 2012b, 2014), we should reiterate that these works employ various simplifying assumptions. In contrast, our approach, which retains all of the terms so as not to bias any particular process over others, is new. Our sample numerical solutions shown in Figures 4, 8 and 12, are the result of such a comprehensive approach. However, since all of the terms contribute to the radiation generation simultaneously, it is not so straightforward to delineate which term is important for the radiation emission at each harmonic. In this regard, the radiation emission at the plasma frequency (fundamental emission), and its harmonics (second and third harmonics) deserves detailed analysis. First, we analyze the radiation emission pattern and angular distribution associated with the fundamental and harmonic emissions.

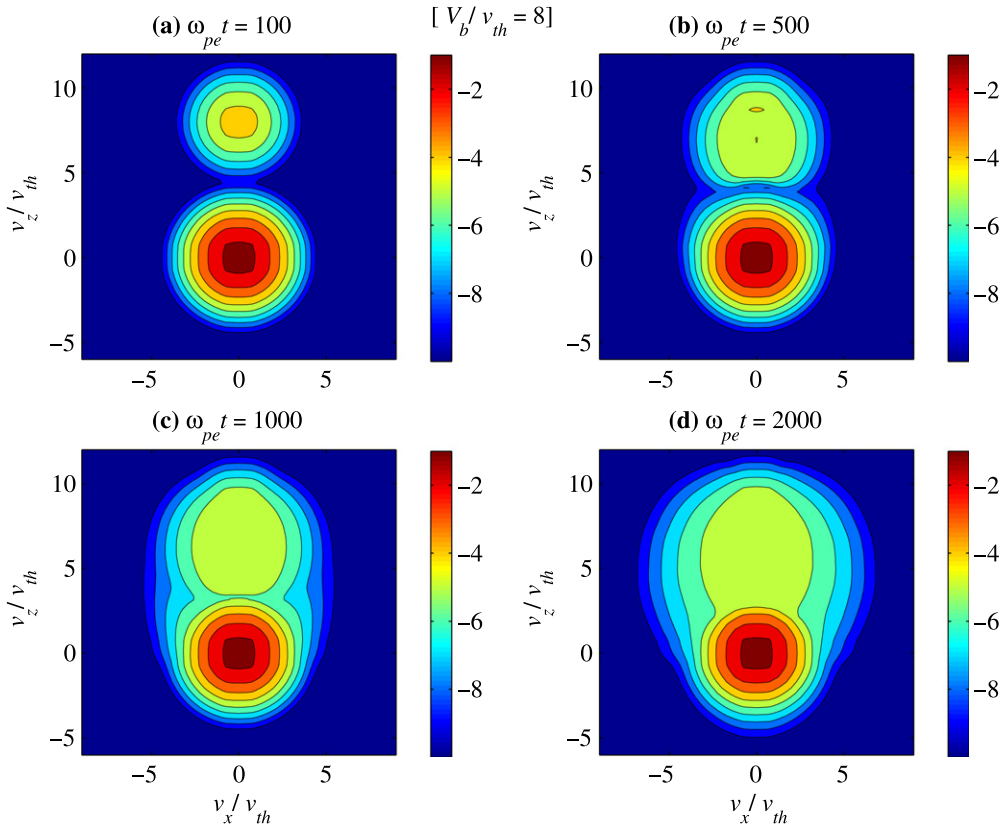

Figure 5. Case 2 ($V_b/v_{\rm th} = 8$): time evolution of the electron velocity distribution function (VDF) F_e (or equivalently Φ_e) vs. $u_\perp = v_x/v_{\rm th}$ and $u_\parallel = v_z/v_{\rm th}$ in filled contour plot format. Panel (a) shows F_e at a relatively early normalized time $\omega_{\rm pe}t = 100$; panel (b) is for $\omega_{\rm pe}t = 500$; panel (c) shows the snapshot at $\omega_{\rm pe}t = 1000$; and the final panel (d) shows evolved F_e at $\omega_{\rm pe}t = 2000$.

3.4. Radiation Emission Pattern for Three Case Studies

In Figure 13 we re-plot the EM radiation spectrum for cases 1 ($V_b/v_{\rm th} = 6$), 2 ($V_b/v_{\rm th} = 8$), and 3 ($V_b/v_{\rm th} = 10$), respectively, at time $\omega_{\rm pe}t = 2 \times 10^3$, which are the same as Figures 4(d), 8(d), and 12(d), respectively, except that we now employ the surface plot format and enlarge the figures into separate panels. This is so as to facilitate the visual examination of the detailed features associated with the radiation emission pattern. Note that even with the enlargement, the radiation intensities still appear somewhat jagged. This is because of the limited resolution in the present numerical computation. In spite of this, the present surface plots help one to understand the overall radiation angular pattern better than the contour plots shown in Figures 4(d), 8(d), and 12(d).

According to (19*b*) and (19*d*), the fundamental emission should be dictated by the three-wave process involving the L mode decaying into the T and S modes (*TdLS*) and the scattering process involving the beating of the L and T modes mediated by the particles (*TsTL*). Of the two processes, the decay mechanism (*TdLS*) is governed by the overall nonlinear coupling coefficient,

$$\frac{(\boldsymbol{q} \times \boldsymbol{q}')^2}{q^2 q'^2} \propto \sin^2 \vartheta. \tag{32}$$

If we associate $\boldsymbol{q}'$ and $z^L_{\boldsymbol{q}'}$ with the Langmuir wave, and $\boldsymbol{q}$ and $z^T_{\boldsymbol{q}}$ with the transverse radiation (which stems from the resonance condition, $\sigma z^T_{\boldsymbol{q}} - \sigma' z^L_{\boldsymbol{q}'} - \sigma'' z^S_{\boldsymbol{q}-\boldsymbol{q}'} = 0$), then if we allow $\boldsymbol{q}'$ vector to lie along the direction of the beam propagation, then it can be seen that the F emission along the direction specified by $\vartheta = 0$ should be prohibited. Of course, the L mode spectrum has a broad range of angles in the present case of 2D physics so that the F emission by the decay process (*TdLS*) is allowed even for $\vartheta = 0$. Nevertheless, Equation (32) predicts that the overall F emission by the decay mechanism should possess a dipolar radiation angular distribution. Indeed, Figure 13 bears such a feature out. Note that the scattering process (19*d*) or (*TsTL*), is also dictated by the same nonlinear coupling coefficient (32), so that the F emission having the dipolar structure with the maximum radiation intensity in directions orthogonal to the direction of the beam propagation direction is consistent.

For the second-harmonic emission, the basic emission mechanism is dictated by (19*a*), or (*TdLL*), with its coupling coefficient,

$$\frac{(\boldsymbol{q} \times \boldsymbol{q}')^2}{q^2 q'^2} \left(q'^2 - \left| \boldsymbol{q} - \boldsymbol{q}' \right|^2 \right)^2$$
$$\sim \sin^2 \vartheta \left(q^2 - 2qq' \cos \vartheta \right)^2 \propto \sin^2 \vartheta \cos^2 \vartheta, \tag{33}$$

where we have identified q with the transverse mode and q' with the Langmuir mode, so that one may approximate $q \ll q'$. According to this picture, the $2H$ emission should possess a quadrupole angular distribution. Indeed, Figure 13(a) shows that the $2H$ emission peaks at a 45° angle (with a symmetric pattern for the negative k_z plane). Note, however, that for higher beam speeds, $V_b/v_{\rm th} = 8$ and 10, the strict quadrupole

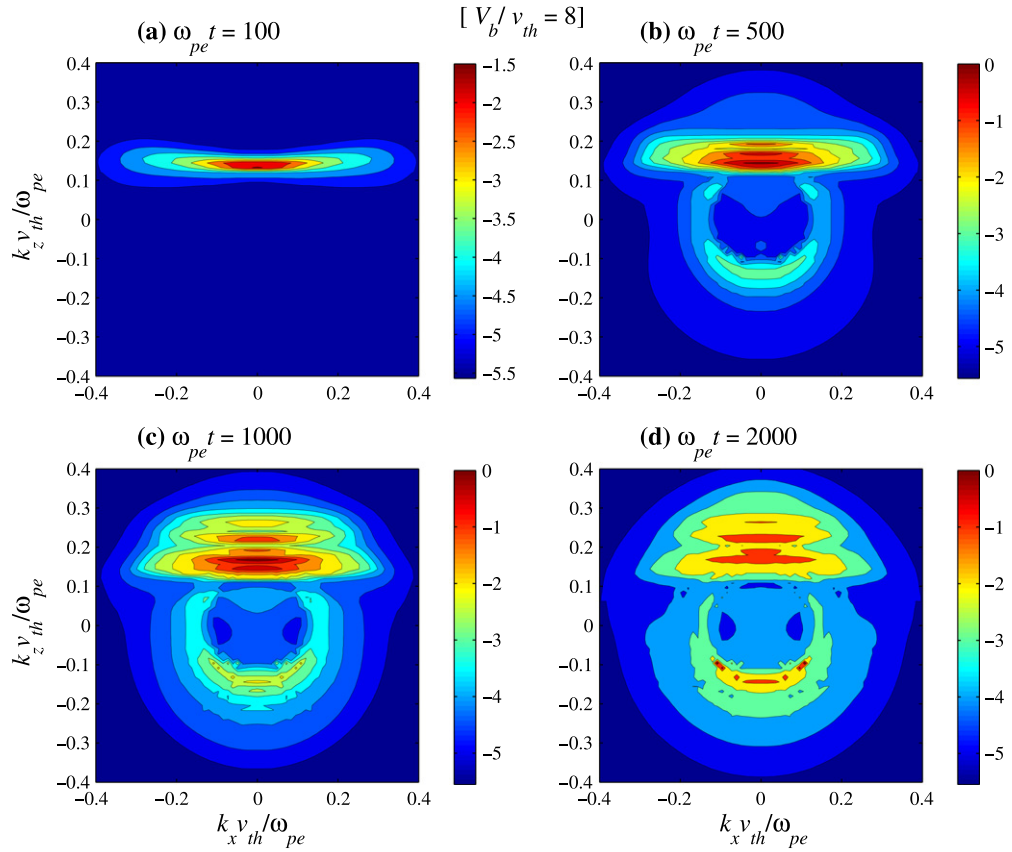

Figure 6. Case 2 ($V_b/v_{\rm th} = 8$): time evolution of the Langmuir wave spectral intensity $I_L(\boldsymbol{k})$ vs. $q_\perp = k_x v_{\rm th}/\omega_{\rm pe}$ and $q_\parallel = k_z v_{\rm th}/\omega_{\rm pe}$. Panel (a) shows $I_L(\boldsymbol{k})$ at $\omega_{\rm pe}t = 100$; panel (b) is for $\omega_{\rm pe}t = 500$; panel (c) is $I_L(\boldsymbol{k})$ at $\omega_{\rm pe}t = 1000$; and the final panel (d) shows $I_L(\boldsymbol{k})$ at $\omega_{\rm pe}t = 2000$.

pattern is no longer identifiable. This is probably owing to the fact that the underlying Langmuir wave spectrum, which is responsible for the second-harmonic emission is not strictly one-dimensional (in fact, it has a finite width in k and is spread out over a semi-arc pattern) such that it is not very meaningful to define one angle ϑ for these cases. Even for case 1, the quadrupole emission is not entirely symmetric with respect to the k_z axis. This is because the system is still evolving at $\omega_{\rm pe}t = 2000$ such that the L mode spectrum has not attained the isotropic pattern yet, which in turn renders the radiation emission in the forward direction to be preferred.

Moving on to the third-harmonic emission for case 3 (and barely visible in case 2), it can be seen that the emission pattern is more or less symmetric. This can be understood from (19*c*), where the nonlinear coupling coefficient that dictates the higher-harmonic emission is given by

$$\left(1 + \frac{(\boldsymbol{q}\cdot\boldsymbol{q}')^2}{q^2 q'^2}\right) \sim 1 + \cos^2\vartheta. \tag{34}$$

As can be seen from this, the higher-harmonic (in this case $3H$) is theoretically predicted to be largely isotropic with some angular dependence, owing to the unity factor on the rhs. Note that the third-harmonic plasma emission associated with the solar type III bursts is only rarely detected (Takakura & Yousef 1974; Brazhenko et al. 2012). There are occasional third-harmonics of type II bursts reported in the literature (Zlotnik et al. 1998). The theory of $3H$ was first developed by Zheleznyakov & Zlotnik (1974), but can also be found in the paper trilogy by Cairns (1987)—see also, Kliem et al. (1992). Of course, our basic theory that allows for $F, 2H, 3H$ as well as even higher-harmonic emission generalizes these theories. Our numerical case studies suggest that $3H$ emission should indeed be rare, and must be associated with an intense electron beam.

3.5. Emission Mechanisms

The wave kinetic Equation (19) contains various terms on the rhs that are responsible for generating the radiation emission at the plasma frequency and its harmonics. When introducing these terms we made the claim that (19*a*) or *TdLL* is responsible for the second-harmonic emission, $L + L \rightarrow T(2H)$, (19*b*) and (19*d*) are responsible for the fundamental emission, $L \rightarrow S + T(F)$ and $L + p \rightarrow T(F)$, respectively, where $p = e, i$, and (19*c*) or $L + T \rightarrow T(3H)$ is the term that leads to the higher-harmonic (frequency higher than $2\omega_{\rm pe}$) emission. This interpretation is intuitively understandable. Upon close examination of the various resonance conditions one may understand why these interpretations make sense. For example, take (19*a*). This term is dictated by the wave–wave interaction involving two L modes, each with a frequency close to $\omega_{\rm pe}$, and a transverse mode. If the two Langmuir wave frequencies are added up, then the resulting T mode should have a frequency close to $2\omega_{\rm pe}$. A similar interpretation can be done for (19*b*) and (19*d*). However, since both (19*b*) and (19*d*) contribute to the fundamental emission, it is important to know which term is more important. This cannot be done by just examining the mathematical structure of

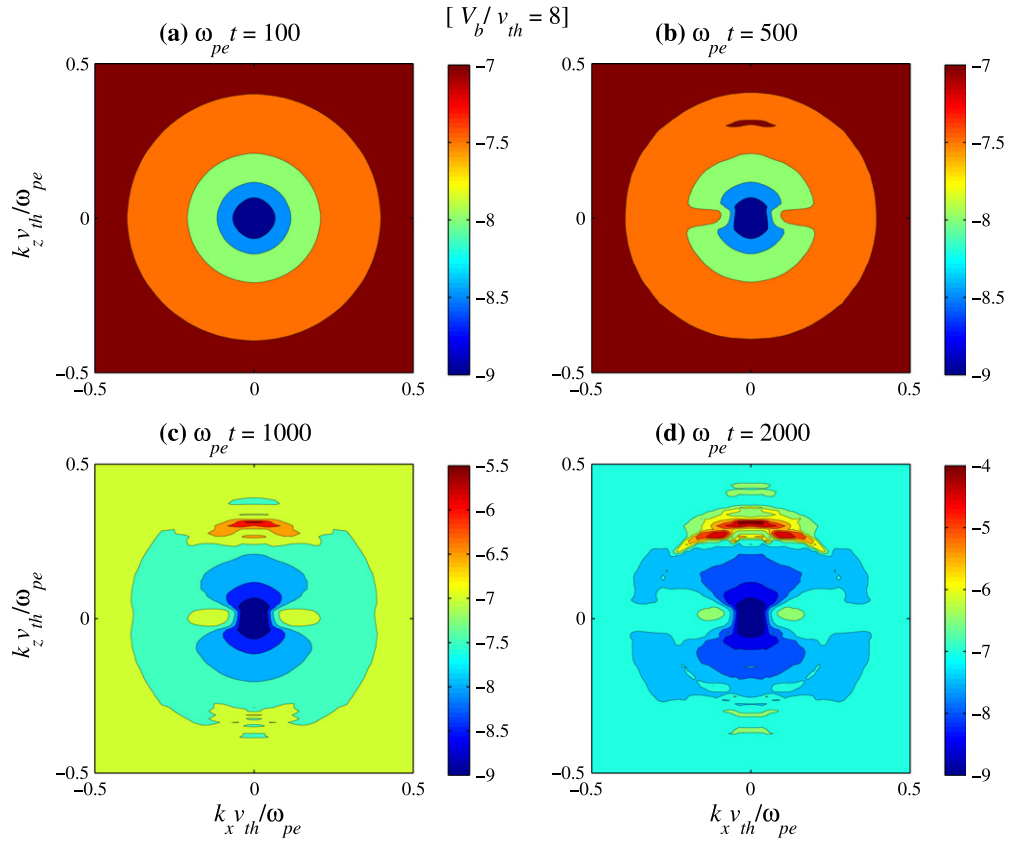

Figure 7. Case 2 ($V_b/v_{\rm th} = 8$): time evolution of the ion-sound wave spectral intensity $I_S(\boldsymbol{k})$ vs. $q_\perp = k_x v_{\rm th}/\omega_{\rm pe}$ and $q_\parallel = k_z v_{\rm th}/\omega_{\rm pe}$. Panel (a) shows $I_S(\boldsymbol{k})$ at $\omega_{\rm pe}t = 100$; panel (b) is for $\omega_{\rm pe}t = 500$; panel (c) is for $\omega_{\rm pe}t = 1000$; and the final panel (d) shows $I_S(\boldsymbol{k})$ at $\omega_{\rm pe}t = 2000$.

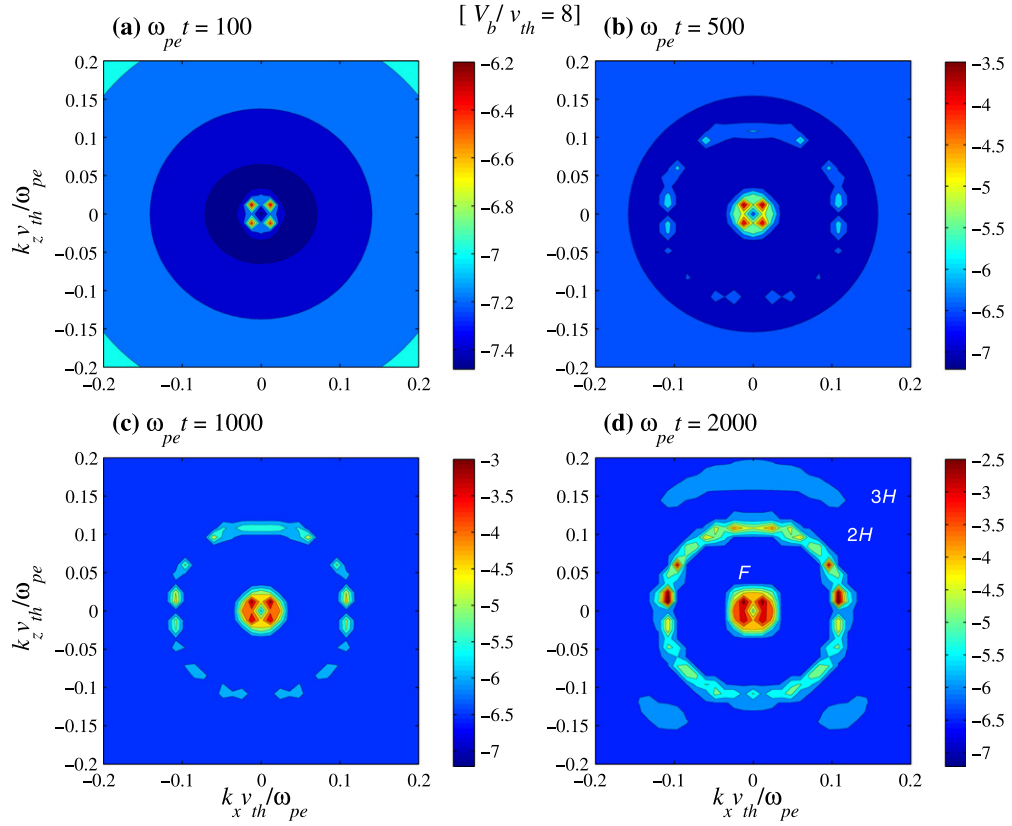

Figure 8. Case 2 ($V_b/v_{\rm th} = 8$): time evolution of the radiation spectral intensity $I_T(\boldsymbol{k})$ vs. $q_\perp = k_x v_{\rm th}/\omega_{\rm pe}$ and $q_\parallel = k_z v_{\rm th}/\omega_{\rm pe}$. Panels (a)–(d) show snapshots of $I_T(\boldsymbol{k})$ at $\omega_{\rm pe}t = 100$, 500, 1000, and $\omega_{\rm pe}t = 2000$.

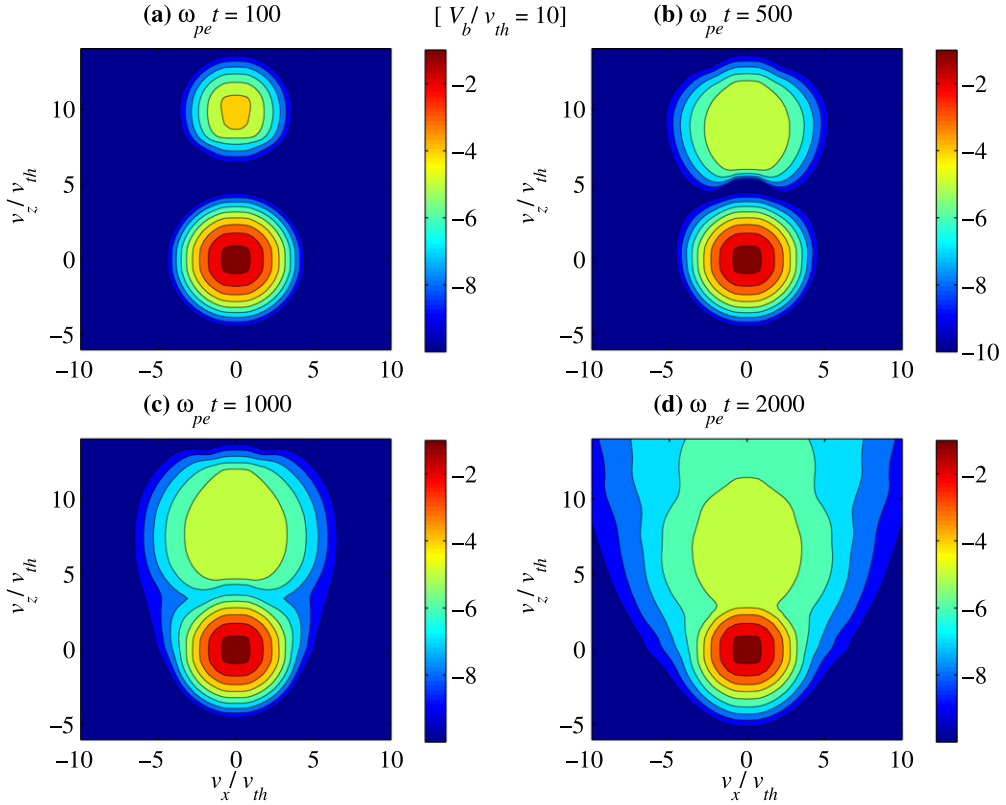

Figure 9. Case 3 ($V_b/v_{\rm th} = 10$): time evolution of the electron velocity distribution function (VDF) F_e (or equivalently Φ_e) vs. $u_\perp = v_x/v_{\rm th}$ and $u_\parallel = v_z/v_{\rm th}$ in filled contour plot format. Panel (a) shows F_e at a relatively early normalized time $\omega_{\rm pe}t = 100$; panel (b) is for $\omega_{\rm pe}t = 500$; panel (c) shows the snapshot at $\omega_{\rm pe}t = 1000$; and the final panel (d) shows the evolved F_e at $\omega_{\rm pe}t = 2000$.

each term. We also made the claim that the background radiation comes primarily from (19*d*). Again, such a claim cannot be verified by just looking at the term. Moreover, we maintained that (19*c*) leads to $3H$ or higher, which is self-evident, but again, in order to quantify the $3H$ mode emission, one must actually solve the equations.

In order to verify all of these, one may solve the basic set of equations by turning each term on and off in the T mode wave kinetic equation, in order to determine the outcome in a quantitative manner. We have paid specific attention to case 3 ($V_b/v_{\rm th} = 10$), since this case led to prominent $3H$ emission as well as F and $2H$ emissions. The result is displayed in Figure 14, where we show for $\omega_{\rm pe}t = 2000$ the normalized electric field spectrum of the T waves as a function of normalized frequency, by integrating $\int d\theta\, q\mathcal{E}_{\boldsymbol{q}}^{\sigma T}$, where $q = (q_\perp^2 + q_\parallel^2)^{1/2}$ and $\theta = \cos^{-1}(q_\parallel/q)$, and by using the dispersion relation for T waves from Equation (21). In panel (a), we show the complete solution in red, and superposed the calculation done by including only the term (19*d*), i.e., the scattering term. The reduced computational result is shown in blue. As one can see, the term *TsLT* produced the peak T mode intensity at the fundamental $\omega \sim \omega_{\rm pe}$, confirming that this term is indeed responsible for generating the F emission. Note also that the term *TsLT* leads to the generation of the background radiation, which is governed by Equation (30) or equivalently, (31). Recall that the background radiation will be present even in the absence of the beam (Ziebell et al. 2014b, 2014c). In short, Figure 14(a) confirms our prediction that the term (19*d*) or *TsLT* is indeed responsible for generating the background radiation as well as producing enhanced radiation emission at the fundamental plasma frequency.

Figure 14(b) compares the full solution (red) against the calculation that includes only term (19*a*) or *TdLL* (blue). In this case, it can be seen that the process of merging of two oppositely traveling L modes into a radiation near $2\omega_{\rm pe}$ is nicely reproduced by the term (19*a*).

Panel (c) of Figure 14 is for comparison between the full solution and the computation including only (19*b*) on the rhs of the T mode equation. As one can appreciate, the process $L \rightarrow S + T(F)$ makes a contribution to the generation of fundamental emission which is almost equal to that of the scattering process, shown in Figure 14(a). This shows that when discussing the F emission, one must include both the decay $L \rightarrow S + T(F)$ and scattering $L + p \rightarrow T(F)$, and ignoring one versus the other may lead to quantitative (if not qualitative) error. Figure 14(c) also shows that the process *TdLS* contributes to the generation of background radiation, but its level is many orders of magnitude lower than that of *TsLT* (panel a). Consequently, our initial claim that (19*d*) or *TsLT* is almost exclusively responsible for the generation of background radiation is verified.

Finally, panel (d) of Figure 14 compares the full solution versus the numerical computation in which only two terms, (19*a*) and (19*c*), or equivalently, *TdLL* + *TdTL*, are included. The purpose of this panel is to understand the role of *TdTL* in generating the third (and higher) harmonics. However, in doing so, including only the term *TdTL* is not a viable way of diagnosing the effects of this term. The reason is because the process $L + T \rightarrow T$ requires the pre-existence of the T mode at

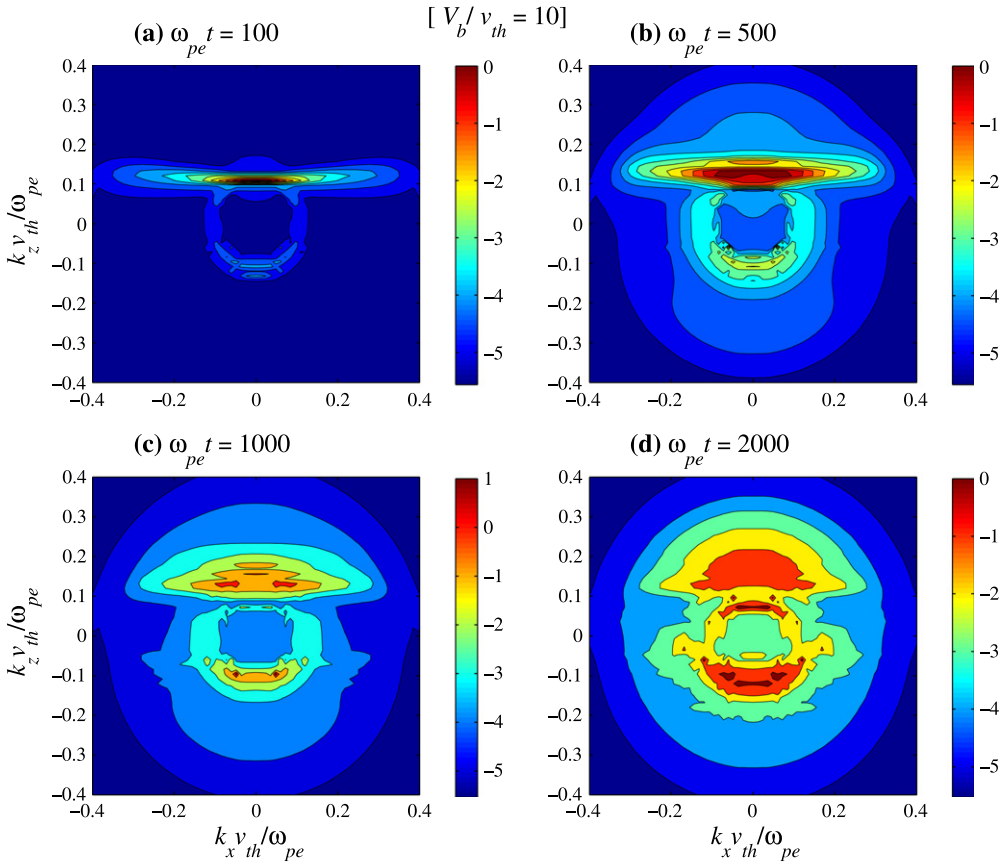

Figure 10. Case 3 ($V_b/v_{\rm th} = 10$): time evolution of the Langmuir wave spectral intensity $I_L(\boldsymbol{k})$ vs. $q_\perp = k_x v_{\rm th}/\omega_{\rm pe}$ and $q_\parallel = k_z v_{\rm th}/\omega_{\rm pe}$. Panel (a) shows $I_L(\boldsymbol{k})$ at $\omega_{\rm pe}t = 100$; panel (b) is for $\omega_{\rm pe}t = 500$; panel (c) is $I_L(\boldsymbol{k})$ at $\omega_{\rm pe}t = 1000$; and the final panel (d) shows $I_L(\boldsymbol{k})$ at $\omega_{\rm pe}t = 2000$.

a lower harmonic frequency. Other processes, namely, $L + p \rightarrow T$, $L + L \rightarrow T$, and $L \rightarrow T + S$ operate on longitudinal modes or the particles. As such, each term alone is sufficient for the diagnostics. However, the process $L + T \rightarrow T$ necessitates the presence of another T mode. For this reason, we kept both terms $TdLL + TdTL$ in the reduced numerical computations.

The result shown in panel (d) shows that the process not only leads to $3H$ emission, but also, interestingly, it contributes somewhat to F emission as well. One can also discern very weak $4H$ emission, which is totally buried under the background radiation so that it becomes undetectable in the full solution. However, the present finding indicates that for an extremely high beam speed (for which, the present weak turbulence formalism is probably inapplicable), the process dictated by $TdTL$ may be capable of high-harmonic EM emission with a harmonic mode number greater than even three. Note that the process responsible for $2H$ emission must be largely $TdLL$, since when we compare panels (b) and (d), the peak around $2\omega_{\rm pe}$ appears the same in both panels, and yet, we know that panel (b) only contains $TdLL$. From this, we may conclude that $TdLL$ is almost exclusively responsible for $2H$ emission, but the term $TdTL$ leads not only to $3H$ emission, but also potentially leads to the $4H$ mode and higher. As a matter of fact, Rhee et al. (2009a, 2009b) employed $V_d/v_{\rm th} = 25$ in their PIC simulation, they managed to obtain up to sixth-harmonic plasma emission. Of course, such a high initial beam speed is probably beyond the applicability of the weak turbulence formalism, but the underlying radiation generation for multiple-harmonic plasma emission is likely owing to the same incoherent Raman process, $L + T \rightarrow T$.

3.6. Effects of Background Radiation

Figure 15 explores the effects of including the background radiation spectrum, Equation (30) or (31), at the outset, versus the computation without such initial radiation intensity. As noted already, the background radiation should be present even in the absence of the beam (Ziebell et al. 2014b, 2014c). Consequently, when we initiate the weak turbulence simulation without the initial radiation level, the system rapidly generates the background radio noise via term (19*d*). Indeed, the upper panel of Figure 15 shows the rapid rise of background radio intensity as the system evolves. The bottom panel shows the same computation, except that we begin the numerical calculation with the asymptotic state of radio noise as the initial spectrum of T waves. As one can see, the background radio spectrum, which is given by an inverse power-law, does not appear to undergo any appreciable change as the dynamics progresses. On top of the background radiation level, however, the free energy associated with the beam leads to enhanced emissions at the first three harmonics.

3.7. Temporal Evolution

Thus far, we have discussed various aspects of the plasma emission process, for instance, by plotting the snapshots of various physical quantities at four time steps during their time

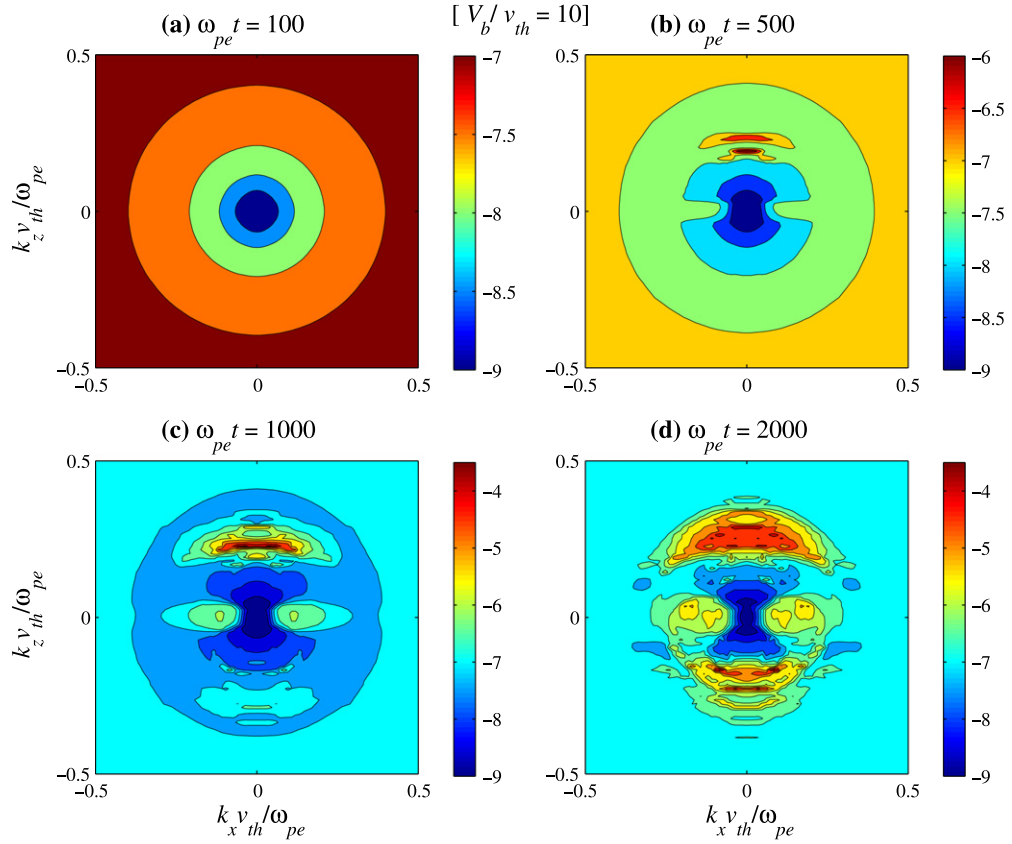

Figure 11. Case 3 ($V_b/v_{\rm th} = 10$): time evolution of the ion-sound wave spectral intensity $I_S(\boldsymbol{k})$ vs. $q_\perp = k_x v_{\rm th}/\omega_{\rm pe}$ and $q_\parallel = k_z v_{\rm th}/\omega_{\rm pe}$. Panel (a) shows $I_S(\boldsymbol{k})$ at $\omega_{\rm pe}t = 100$; panel (b) is for $\omega_{\rm pe}t = 500$; panel (c) is for $\omega_{\rm pe}t = 1000$; and the final panel (d) shows $I_S(\boldsymbol{k})$ at $\omega_{\rm pe}t = 2000$.

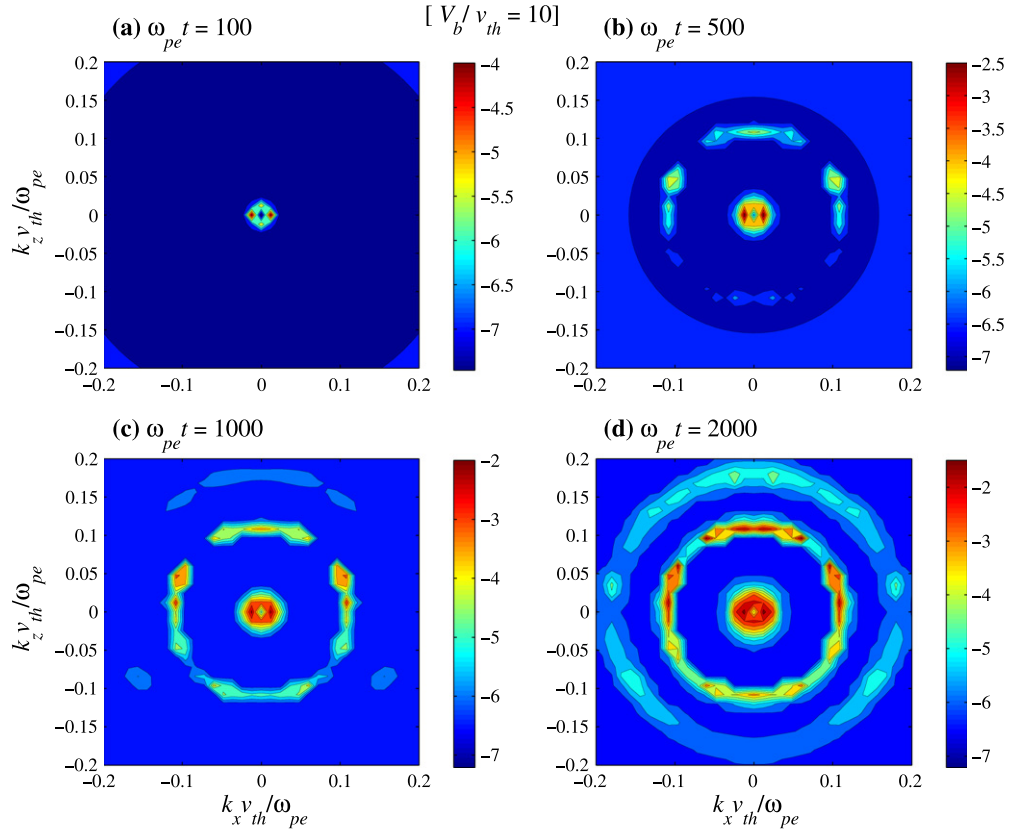

Figure 12. Case 3 ($V_b/v_{\rm th} = 10$): time evolution of the radiation spectral intensity $I_T(\boldsymbol{k})$ vs. $q_\perp = k_x v_{\rm th}/\omega_{\rm pe}$ and $q_\parallel = k_z v_{\rm th}/\omega_{\rm pe}$. Panels (a)–(d) show snapshots of $I_T(\boldsymbol{k})$ at $\omega_{\rm pe}t = 100$, 500, 1000, and $\omega_{\rm pe}t = 2000$.

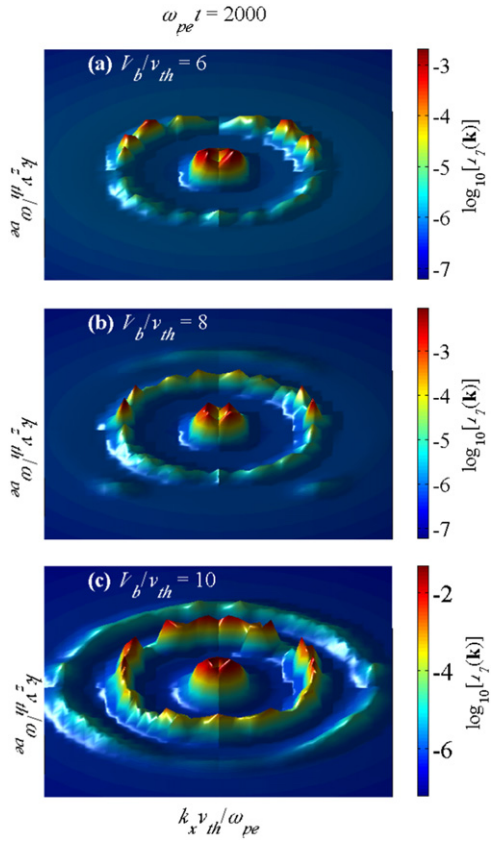

Figure 13. Radiation emission pattern for all three cases at $\omega_{pe}t = 2 \times 10^3$.

evolution and by carrying out a detailed analysis of various radio emission mechanisms by turning certain terms in the T mode wave kinetic equation on and off. Before we close the present discussion, however, we now consider the overall time evolution of integrated wave intensities for each wave mode. Specifically, we now plot in Figure 16, the total L mode wave energy, $\int d\boldsymbol{k} I_L(\boldsymbol{k})$, the S mode wave energy, $\int d\boldsymbol{k} I_S(\boldsymbol{k})$, and the radiation wave energy, $\int d\boldsymbol{k} I_T(\boldsymbol{k})$. For the radiation energy, we plot two cases, one without the initial radiation level, and the other with the initial noise—Figure 16(c) and (d). Specifically, Figure 16(a) shows the normalized Langmuir wave energy density $\int d\boldsymbol{k} I_L(\boldsymbol{k})$ (where the normalization factor is implicit) versus normalized time $\tau = \omega_{pe}t$, for three different initial beam speeds, $V_b/v_{th} = 6$ (blue), 8 (red), and 10 (black). Figure 16(b) plots the normalized ion-sound wave energy density $\int d\boldsymbol{k} I_S(\boldsymbol{k})$ in the same format. Figure 16(c) displays the total radiation energy $\int d\boldsymbol{k} I_T(\boldsymbol{k})$ in the case when there is no initial radiation energy. Finally, Figure 16(d) plots the same radiation energy $\int d\boldsymbol{k} I_T(\boldsymbol{k})$, except that in this case, we began the computation with a finite background radiation level as dictated by Equation (30) or (31).

Figure 16 shows that the generation of Langmuir turbulence via bump-on-tail instability is the first and fastest process in the entire course of plasma emission physics. Very early on, the Langmuir waves exponentially grow, followed by saturation. This is expected. However, what was not expected, at least on the basis of intuition, is that the generation of radiation energy is more rapid than the production of ion-sound turbulence by the nonlinear decay process. This is because the customary expectation is that the plasma emission should manifest itself only at the late nonlinear stage of the mode–mode coupling process. Note that the 2D PIC EM simulation by Kasaba et al. (2001) compares the time rate of change in the wave energy associated with the Langmuir turbulence and second-harmonic ($2H$) radiation energy. Their Figure 3, for instance, compares reasonably well with Figure 16, at least in the qualitative sense. A similar comparison between the electrostatic Langmuir-wave growth and the radiation wave energy for $2H$, $3H$, and $4H$ modes can also be found in the simulation paper by Rhee et al. (2009a)—see their Figure 5. However, neither of these papers compared the simulation results against the ion-sound wave growth behavior. As a consequence, it was not possible to discern whether the radiation production was faster than the ion-sound mode generation or not. The present investigation shows that the radiation energy production closely follows the Langmuir turbulence generation, and surprisingly, the ion-sound turbulence takes place only with some significant time lag. Such a finding, which could not have been predicted a priori, is new.

Note that the two alternate cases of computational scheme, namely one without the initial radiation noise and the other with the background noise already in place, show qualitatively similar results in the long run, but the initial temporal behaviors for the two cases are obviously quite different. In the case without the initial noise, the finite radiation energy is almost immediately generated, according to the dictates of Equation (19*d*). In contrast, when the initial radiation energy is already present at the noise level, the generation of EM radiation takes place in a manner that is expected of the typical nonlinear instability process. That is, only after the Langmuir wave intensity exceeds a certain threshold value does the radiation get generated.

In Figure 17, we plot the temporal evolution of each of the EM harmonic modes. The left-hand panels designated by (a) show the time evolution of normalized radiation energy $\int d\boldsymbol{k} I_T(\boldsymbol{k})$ for each harmonic mode, versus normalized time $\omega_{pe}t$, for the case when there is no initial radiation. Blue, red, and black curves show the temporal behavior associated with the fundamental (F), second-harmonic ($2H$), and third-harmonic ($3H$) modes. From top to bottom, sub-panels (a.1), (a.2), and (a.3) correspond to initial beam speeds $V_b/v_{th} = 6$, 8, and 10, respectively. The right-hand panels (b) are the same as the left-hand panels, except that the results correspond to the runs with initial background radiation already present.

EM PIC simulations by Kasaba et al. (2001) and Rhee et al. (2009a) only show temporal development of harmonic modes $2H$ and higher. This is because their simulation setup could not resolve the fundamental emission sufficiently well. Note that the fundamental mode is in the very close vicinity of the cutoff frequency such that their wavelength is extremely long. The PIC numerical simulation cannot quite resolve such a long wavelength mode, whereas the present EM weak turbulence theory, which operates on Fourier space, has no intrinsic difficulty in dealing with the fundamental emission. If we exclude the fundamental mode, the overall behavior of the second-harmonic mode growing faster than the third-harmonic is consistent with the simulations by Kasaba et al. (2001) and Rhee et al. (2009a). The new finding according to the present paper is that the fundamental emission takes place before

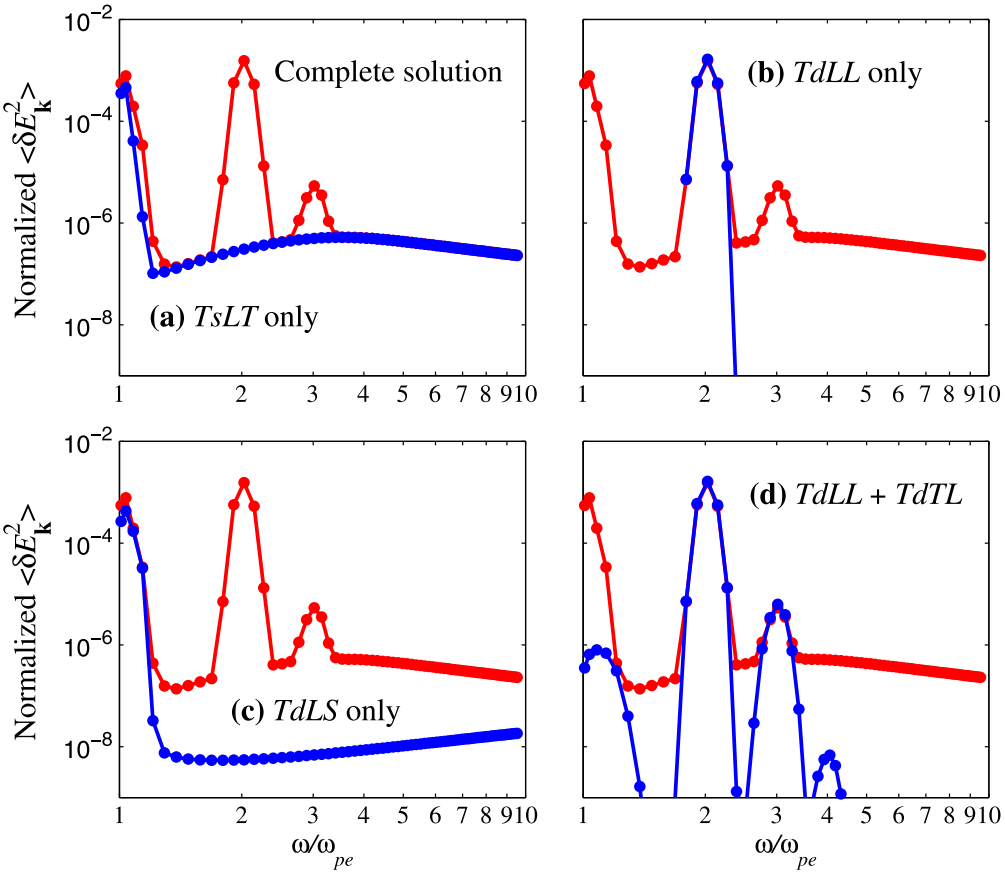

Figure 14. Radiation emission intensity vs. normalized frequency, for the case $V_b/v_{\rm th} = 10.0$, computed on the basis of Equation (19) by including certain terms only and artificially turning other term off in order to test the radiation mechanism (blue curves). The full solution is also shown, for comparison (red curves). The results are shown for normalized time $\omega_{\rm pe}t = 2000$, using logarithmic scale. Panel (a) includes only term (19*d*) or *TsTL*; panel (b) includes term (19*a*) or *TdLL*; panel (c) is for (19*b*) or *TdLS*; and panel (d) is for computation including (19*a*) and (19*c*), or *TdLL* + *TdTL*.

higher-harmonic modes (see especially, the right-hand panels). It is also interesting to note that although, initially, the fundamental mode grows faster and reaches higher radiation intensity, the second-harmonic mode, which grows later, eventually takes over and attains a higher radiation level, at least for cases 2 and 3 (i.e., $V_b/v_{\rm th} = 8$ and 10, respectively), although even for case 1 ($V_b/v_{\rm th} = 6$), one may surmise that eventually $2H$ will overtake F mode had we ran the code for a longer time.

The issue of whether the type III bursts are made of the F or H component is an unresolved issue in the literature (Dulk et al. 1984; Robinson & Cairns 1998b). If our case studies are any guide, we believe that the harmonic component will eventually dominate over the fundamental in the long run. Indeed, Figure 9 of the paper by Dulk et al. (1984) shows that schematically, the fundamental manifests itself first, but later, the harmonic component dominates, which is a conclusion derived from observations. This appears to be consistent with Figure 17.

4. SUMMARY

The present paper is a follow-up of a recent Letter (Ziebell et al. 2014a) that reported the first-ever theoretical demonstration of F/H pair emission starting from the beam-plasma instability by allowing all of the relevant nonlinear processes to operate within the EM weak turbulence formalism. Because of the limited scope of the Letter format, many details associated with our numerical computation could not be discussed therein. The purpose of the present paper has been to greatly expand the discussion. We have accomplished this by first displaying all of the necessary theoretical Equations (1)–(14) and their normalized forms (15)–(22), so that an interested reader may reproduce our results on the basis of the equations displayed in the present paper.

We have then laid out the numerical scheme as well as initial configurations, followed by three case studies. We adopted three different electron beam speeds, $V_b/v_{\rm th} = 6$, 8, and 10, and displayed the snapshots of the electron VDF, Langmuir, ion-sound, and radiation spectra at four different time intervals each (Figures 1–12). We then re-examined the radiation angular pattern in Figure 13 and compared the numerical outcome against theoretical predictions.

An important discussion that followed involved the detailed identification of the radiation emission mechanisms responsible for generating the plasma emission at each harmonic. By turning certain terms on the rhs of the T mode wave kinetic equations on and off, we have clearly identified the basic radiation mechanism that leads to the fundamental and higher-harmonic emissions (Figure 14).

Figure 15 compared the two runs, one without any initial radiation intensity, and the other with a finite radiation background at $t = 0$. The presence of the background radiation was recently predicted and confirmed by the PIC simulation

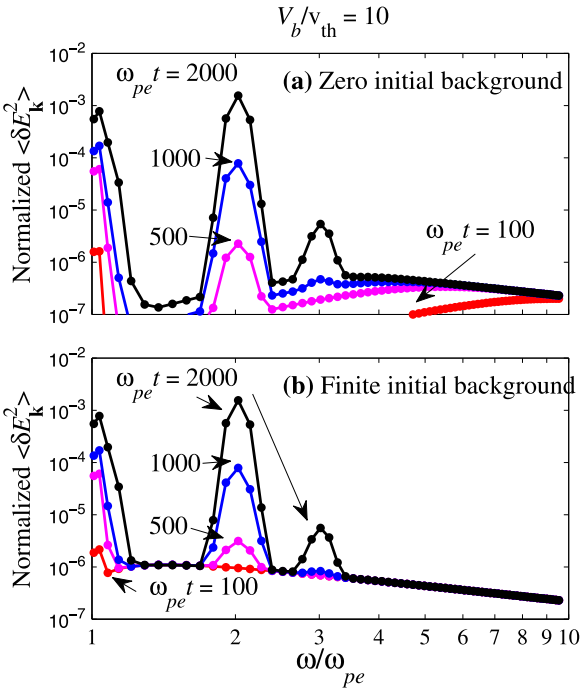

Figure 15. Upper panel shows the temporal development of the normalized electric field intensity $\langle \delta E^2(\boldsymbol{k})\rangle$ vs. normalized frequency ω/ω_{pe} for initial beam speed $V_b/v_{th} = 10$ (case 3), when we do not impose any initial transverse mode intensity (logarithmic scale). Panel (b) is the same except that we start the numerical computation with the background radiation, Equation (30) or (31).

(Ziebell et al. 2014b, 2014c). In the subsequent two Figures (16 and 17), we investigated the temporal evolution of the wave energy associated with longitudinal and transverse modes, but we carried out two different runs according to the scheme in Figure 15, namely, with or without the initial background noise. It was found that even if the system was initiated without the radio noise, the plasma quickly generates the background radiation. One of the most interesting findings is that the radiation actually grows faster than the ion-sound turbulence generation timescale. We also unveiled an interesting fact that the plasma emission should be first dominated by the fundamental emission, but over time, the second-harmonic component should eventually overtake the fundamental, which implies that most of the type III bursts should be at the harmonic. Finally, we found that the generation of the third harmonic should be associated with intense electron beams and should be very rare. Our finding implies that although the fourth and higher harmonics are not impossible, their intensities should be extremely weak such that they are unlikely to be detectable, especially when occulted by the background radiation level.

This work has been partially supported by the Brazilian agencies CNPq and FAPERGS. P.H.Y. acknowledges NSF grant AGS1242331 and the BK21 plus a grant from the National Research Foundation (NRF) of the Republic of Korea.

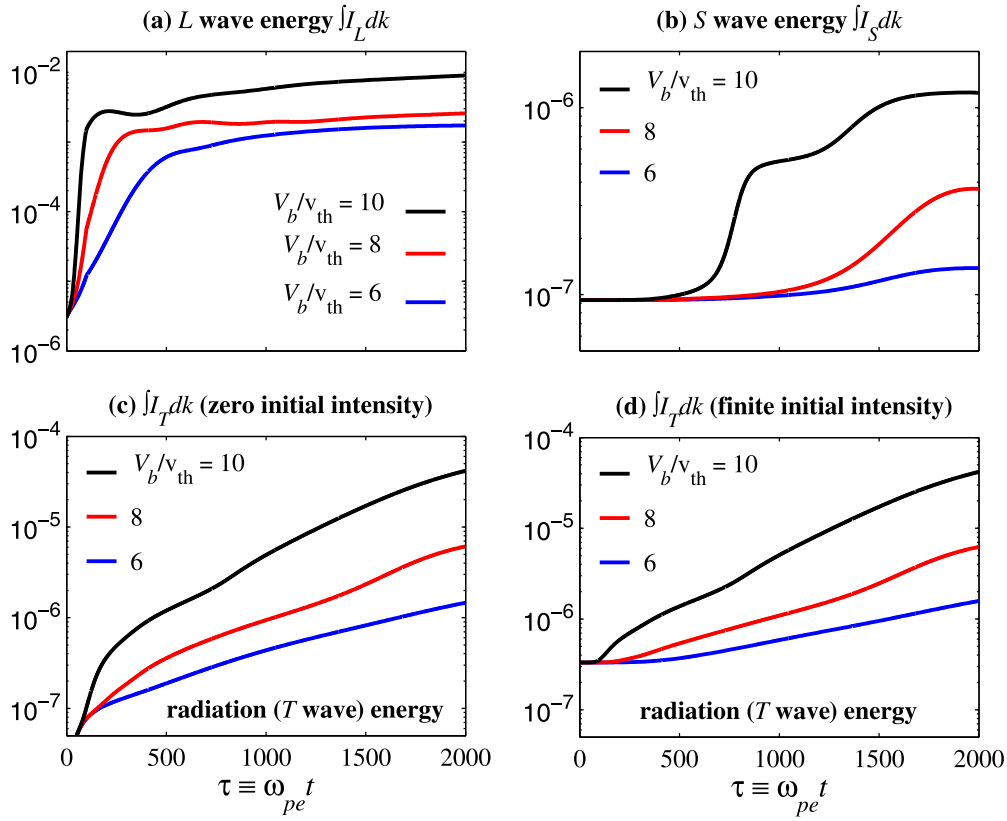

Figure 16. Panel (a) shows the time evolution of integrated normalized Langmuir wave intensity $\int d\boldsymbol{k} I_L(\boldsymbol{k})$ vs. normalized time $\tau = \omega_{pe}t$ for three different initial beam speeds $V_b/v_{th} = 6$, 8, and 10 (logarithmic scale); panel (b) corresponds to the ion-sound wave energy $\int d\boldsymbol{k} I_S(\boldsymbol{k})$ in the same format; panel (c) is for the total radiation energy $\int d\boldsymbol{k} I_T(\boldsymbol{k})$ in the case when there is no initial radiation energy; while panel (d) is the same radiation energy $\int d\boldsymbol{k} I_T(\boldsymbol{k})$ when there exists a finite background radiation level.

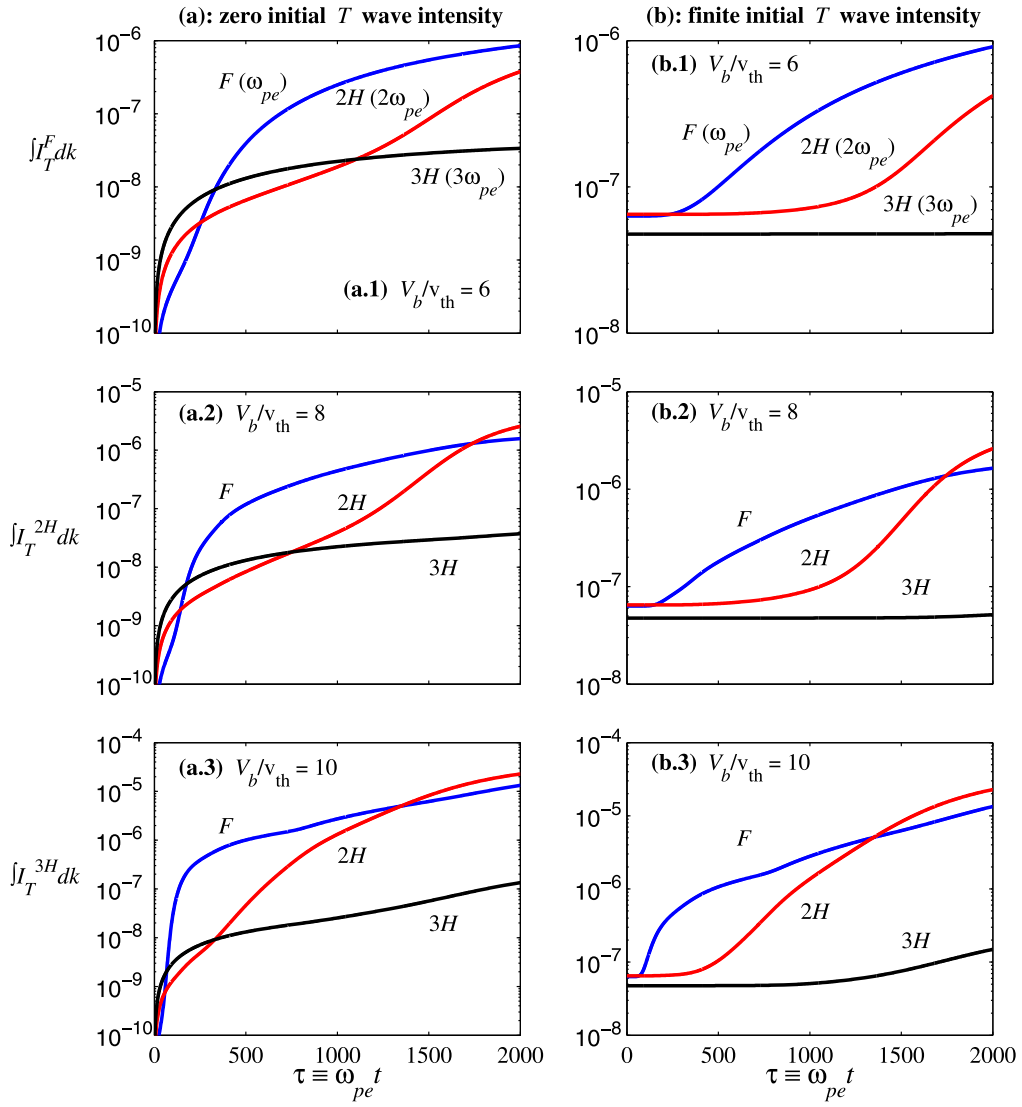

Figure 17. Left-hand panels (a) show the time evolution of normalized radiation energy $\int d\boldsymbol{k} I_T(\boldsymbol{k})$ vs. normalized time $\omega_{\rm pe}t$, for the case when there is no initial radiation. Blue, red, and black curves show the temporal behavior associated with the fundamental (F), second-harmonic ($2H$), and third-harmonic ($3H$) modes. From top to bottom, sub-panels (a.1), (a.2), and (a.3) correspond to initial beam speeds $V_b/v_{\rm th} = 6$, 8, and 10, respectively, using a logarithmic scale. The right-hand panels (b) are the same as the left-hand panels, except that the results correspond to the runs with initial background radiation already present.

REFERENCES

Brazhenko, A. I., Melnik, V. N., Konovalenko, A. A., et al. 2012, OAP, 25, 181
Cairns, I. H. 1987, JPlPh, 38, 169
Cane, H. V., Erickson, W. C., & Prestage, N. P. 2002, JGR, 107, 1315
Dulk, G. A. 1985, ARA&A, 23, 169
Dulk, G. A., Steinberg, J. L., & Hoang, S. 1984, A&A, 141, 30
Ergun, R. E., Larson, D., Lin, R. P., et al. 1998, ApJ, 503, 435
Fainberg, J., & Stone, R. G. 1974, SSRv, 16, 145
Foroutan, G., Robinson, P. A., Zahed, H., & Cairns, I. H. 2007, PhPl, 14, 122902
Frank, L. A., & Gurnett, D. A. 1972, SoPh, 27, 446
Ganse, U., Kilian, P., Spanier, F., & Vainio, R. 2012a, ApJ, 751, 145
Ganse, U., Kilian, P., Vainio, R., & Spanier, F. 2012b, SoPh, 280, 551
Ginzburg, C. L., & Zheleznyakov, V. V. 1958, Sov. Astron.-AJ, 2, 653
Goldman, M. V. 1983, SoPh, 89, 403
Goldman, M. V., & Dubois, D. F. 1982, PhFl, 25, 1062
Gosling, J. T., Skoug, R. M., & McComas, D. J. 2003, GeoRL, 30, 1697
Goldstein, M. L., Smith, R. A., & Papadopoulos, K. 1979, ApJ, 234, 683
Grognard, R. J.-M. 1980, in IAU Symp. 86, Radio Physics of the Sun, ed. M. R. Kundu & T. E. Gergely (Dordrecht: Reidel), 303
Grognard, R. J.-M. 1982, SoPh, 81, 173
Grognard, R. J.-M. 1985, in Solar Radiophysics, ed. D. J. McLean, & N. R. Labrum (New York: Cambridge Univ. Press), 253
Gurnett, D. A., Marsch, E., Pilipp, W., Schwenn, R., & Rosenbauer, H. 1979, JGR, 84, 2029
Kane, S. R. 1972, SoPh, 27, 174
Kaplan, S. A., & Tsytovich, V. N. 1968, Sov. Astron.-AJ, 11, 956
Karlicky, M., & Vandas, M. 2007, P&SS, 55, 2336
Kasaba, Y., Matsumoto, H., & Omura, Y. 2011, JGR, 106, 18693
Kliem, B., Krueger, A., & Treumann, R. A. 1992, SoPh, 140, 149
Kontar, E. P. 2001a, SoPh, 202, 131
Kontar, E. P. 2001b, A&A, 375, 629
Kontar, E. P. 2001c, PPCF, 43, 589
Kontar, E. P., & Pécseli, H. L. 2002, PhRvE, 65, 066408
Krucker, S., Kontar, E. P., Christe, S., & Lin, R. P. 2007, ApJL, 663, L109
Kundu, M. R. 1965, Solar Radio Astronomy (New York: Interscience)
Li, B., Cairns, I. H., & Robinson, P. A. 2008a, JGR, 113, A06104
Li, B., Cairns, I. H., & Robinson, P. A. 2008b, JGR, 113, A06105
Li, B., Cairns, I. H., & Robinson, P. A. 2009, JGR, 114, A02104
Li, B., Cairns, I. H., & Robinson, P. A. 2010, A&A, 510, L6
Li, B., Cairns, I. H., & Robinson, P. A. 2011b, ApJ, 730, 20
Li, B., Cairns, I. H., & Robinson, P. A. 2011c, ApJ, 730, 21
Li, B., Cairns, I. H., Yan, Y. H., & Robinson, P. A. 2011a, ApJL, 738, L9
Li, B., Robinson, P. A., & Cairns, I. H. 2006a, PhRvL, 96, 145005

Li, B., Robinson, P. A., & Cairns, I. H. 2006b, PhPl, 13, 092902
Li, B., Robinson, P. A., & Cairns, I. H. 2006c, PhPl, 13, 082305
Li, B., Willes, A. J., Robinson, P. A., & Cairns, I. H. 2003, PhPl, 10, 2748
Li, B., Willes, A. J., Robinson, P. A., & Cairns, I. H. 2005a, PhPl, 12, 052324
Li, B., Willes, A. J., Robinson, P. A., & Cairns, I. H. 2005b, PhPl, 12, 012103
Lin, R. P. 1970, SoPh, 12, 266
Lin, R. P. 1973, ApJL, 14, 191
Lin, R. P. 1974, SSRv, 16, 189
Lin, R. P., Anderson, K. A., & Cline, T. L. 1972, PhRvL, 29, 1035
Lin, R. P., Larson, D., McFadden, J., et al. 1996, GeoRL, 23, 1211
Lin, R. P., Levedahl, W. K., Lotko, W., Gurnett, D. A., & Scarf, F. L. 1986, ApJ, 308, 954
Lin, R. P., Potter, D. W., Gurnett, D. A., & Scarf, F. L. 1981, ApJ, 251, 364
Magelssen, G. R., & Smith, D. F. 1977, SoPh, 55, 211
Melrose, D. B. 1980a, Plasma Astrophysics, Vol. 1 and 2 (New York: Gordon and Breach)
Melrose, D. B. 1980b, SSRv, 26, 3
Melrose, D. B. 1982, AuJPh, 35, 67
Melrose, D. B. 1986, Instabilities in Space and Laboratory Plasmas (New York: Cambridge Univ. Press)
Melrose, D. B. 1987, SoPh, 111, 89
Mel'nik, V. N., Kontar, E. P., & Lapshin, V. I. 1999, SoPh, 196, 199
Muschietti, L. 1990, SoPh, 130, 201
Newbury, J. A., Russell, C. T., Phillips, J. L., & Gary, S. P. 1998, JGR, 103, 9553
Papadopoulos, K., Goldstein, M. L., & Smith, R. A. 1974, ApJ, 190, 175
Papadopoulos, K., et al. 1975, PhPl, 18, 1769
Ratcliffe, H., Bian, N. H., & Kontar, E. P. 2012, ApJ, 761, 176
Reid, H. A. S., & Ratcliffe, H. 2014, RAA, 14, 773
Reiner, M. J., Goetz, K., Fainberg, J., et al. 2009, SoPh, 259, 255
Reiner, M. J., Stone, R. G., & Fainberg, J. 1992, ApJ, 394, 340
Rha, K., Ryu, C.-M., & Yoon, P. H. 2013, ApJL, 775, L21
Rhee, T., Ryu, C.-M., Woo, M., et al. 2009a, ApJ, 694, 618
Rhee, T., Woo, M., & Ryu, C.-M. 2009b, JKPS, 54, 313
Roberts, J. A. 1959, AuJPh, 12, 327
Robinson, P. A., & Cairns, I. H. 1998a, SoPh, 181, 363
Robinson, P. A., & Cairns, I. H. 1998b, SoPh, 181, 395
Robinson, P. A., & Cairns, I. H. 1998c, SoPh, 181, 429
Rosenberg, H. 1976, Phil. Trans. R. Soc. London, Ser. A., 281, 461
Schmidt, J. M., & Cairns, I. H. 2012a, JGR, 117, A04106
Schmidt, J. M., & Cairns, I. H. 2012b, JGR, 117, A11104
Schmidt, J. M., & Cairns, I. H. 2014, JGR, 119, 69
Smerd, S. F. 1976, SoPh, 46, 493
Smith, R. A., Goldstein, M. L., & Papadopoulos, K. 1979, ApJ, 234, 348
Stewart, R. T. 1974, in Proc. IAU Symp. No. 57, Coronal Disturbances, ed. G. Newkirk (Dordrecht: Reidel), 161
Sturrock, P. A. 1964, in Proc. AAS–NASA Symp. Physics of Solar Flares, ed. W. N. Hess (Washington, DC: Government Press), 357
Suzuki, S., & Dulk, G. A. 1985, in Solar Radiophysics, ed. D. J. McLean, & N. R. Labrum (New York: Cambridge Univ. Press), 289
Takakura, T., & Yousef, S. 1974, SoPh, 36, 451
Takakura, T., & Shibahashi, H. 1976, SoPh, 46, 323
Tsytovich, V. N. 1967, SvPhU, 9, 805
Wang, L., Lin, R. P., Krucker, S., & Mason, G. M. 2012, ApJ, 759, 69
Wild, J. P. 1950a, AuSRA, 3, 387
Wild, J. P. 1950b, AuSRA, 3, 541
Wild, J. P., & McCready, L. L. 1950, AuSRA, 3, 399
Wild, J. P., Murray, J. D., & Rowe, W. C. 1954, AuJPh, 7, 439
Wild, J. P., Sheridan, K. V., & Neylan, A. A. 1959, AuJPh, 12, 369
Wild, J. P., & Smerd, S. F. 1972, ARA&A, 10, 159
Wild, J. P., Smerd, S. F., & Weiss, A. A. 1963, ARA&A, 1, 291
Yoon, P. H. 2000, PhPl, 7, 4858
Yoon, P. H. 2005, PhPl, 12, 042306
Yoon, P. H. 2006, PhPl, 13, 022302
Yoon, P. H., Hong, H., Kim, S., et al. 2012b, ApJ, 755, 112
Yoon, P. H., Ziebell, L. F., Gaelzer, R., & Pavan, J. 2012a, PhPl, 19, 102303
Zaitsev, V. V., Mityakov, N. A., & Rapoport, V. O. 1972, SoPh, 24, 444
Zheleznyakov, V. V. 1970, Radio Emission of the Sun and Planets (New York: Pergamon)
Zheleznyakov, V. V., & Zaitsev, V. V. 1970a, Sov. Astron.-AJ, 14, 250
Zheleznyakov, V. V., & Zaitsev, V. V. 1970b, Sov. Astron.-AJ, 14, 47
Zheleznyakov, V. V., & Zlotnik, E. Ya. 1974, SoPh, 36, 451
Ziebell, L. F., Gaelzer, R., Pavan, J., & Yoon, P. H. 2008a, PPCF, 50, 085011
Ziebell, L. F., Gaelzer, R., & Yoon, P. H. 2001, PhPl, 8, 3982
Ziebell, L. F., Gaelzer, R., & Yoon, P. H. 2008b, PhPl, 15, 032303
Ziebell, L. F., Yoon, P. H., Gaelzer, R., & Pavan, J. 2012, PPCF, 54, 055012
Ziebell, L. F., Yoon, P. H., Gaelzer, R., & Pavan, J. 2014a, ApJL, 795, L32
Ziebell, L. F., Yoon, P. H., Gaelzer, R., & Pavan, J. 2014c, PhPl, 21, 012306
Ziebell, L. F., Yoon, P. H., Pavan, J., & Gaelzer, R. 2011a, ApJ, 727, 16
Ziebell, L. F., Yoon, P. H., Pavan, J., & Gaelzer, R. 2011b, PPCF, 53, 085004
Ziebell, L. F., Yoon, P. H., Simões, F. J. R., Gaelzer, R., & Pavan, J. 2014b, PhPl, 21, 010701
Zlotnik, E. Ya., Klassen, A., Klein, K.-L., Aurass, H., & Mann, G. 1998, A&A, 331, 1087